AGU PUBLICATIONS

JGR

Journal of Geophysical Research: Oceans

RESEARCH ARTICLE

10.1002/2013JC009274

Large-scale impact of Saharan dust on the North Atlantic Ocean circulation

N. Serra[1], N. Martínez Avellaneda[2], and D. Stammer[1]

[1]Institut für Meereskunde, Centrum für Erdsystemforschung und Nachhaltigkeit, University of Hamburg, Germany, [2]Now at Climate, Atmosphere Science and Physical Oceanography, Scripps Institution of Oceanography, University of California San Diego, La Jolla, California, USA

Key Points:
- Saharan dust induced forcing is simulated by idealized radiation anomalies
- Significant impacts on North Atlantic gyre and overturning circulations

Correspondence to:
N. Serra,
nuno.serra@zmaw.de

Citation:
Serra, N., N. M. Avellaneda, and D. Stammer (2014), Large-scale impact of Saharan dust on the North Atlantic Ocean circulation, *J. Geophys. Res. Oceans*, *119*, 704–730, doi:10.1002/2013JC009274.

Received 15 JULY 2013
Accepted 6 JAN 2014
Published online 4 FEB 2014

Abstract The potential for a dynamical impact of Saharan mineral dust on the North Atlantic Ocean large-scale circulation is investigated. To this end, an ocean general circulation model forced by atmospheric fluxes is perturbed by an idealized, seasonally varying, net shortwave flux anomaly, as it results from remote sensing observations of aerosol optical thickness representing Saharan dust load in the atmosphere. The dust dynamical impact on the circulation is assessed through a comparison between perturbed and an unperturbed run. Results suggest that, following the dust-induced shortwave irradiance anomaly, a buoyancy anomaly is created in the Atlantic offshore the African coast, which over the course of the time propagates westward into the interior Atlantic while progressively subducting. Changes in the large-scale barotropic and overturning circulations are significant after 3 years, which coincides with the elapsed time required by the bulk of the buoyancy perturbation to reach the western boundary of the North Atlantic. Although small in amplitude, the changes in the meridional overturning are of the same order as interannual-to-decadal variability. Variations in the amplitude of the forcing lead to changes in the amplitude of the response, which is almost linear during the first 3 years. In addition, a fast, but dynamically insignificant, response can be observed to propagate poleward along the eastern boundary of the North Atlantic, which contributes to a nonlinear response in the subpolar region north of 40°N.

1. Introduction

The presence of Saharan mineral dust in the North Atlantic has important implications for the atmospheric radiative balance and ocean circulation. It has been shown that an enhanced load of Saharan mineral dust in the atmosphere can lead to a cooling of the Atlantic sea surface temperature (SST) due to the attenuation (scattering and absorption) of solar radiation in the dust layer and an associated reduction of shortwave radiation reaching the sea surface [e.g., *Lau and Kim*, 2007; *Foltz and McPhaden*, 2008a; *Martínez Avellaneda et al.*, 2010; *Yue et al.*, 2011]. On the other hand, the Saharan Air Layer (SAL), in which the mineral dust aerosol is embedded, brings warm and dry air conditions to the tropical Atlantic, modifying the meridional air temperature gradient aloft in the region and giving rise to an intensification of easterly winds in the northern part of the African Easterly Jet. As a consequence, and despite the cool radiative-induced response in SST, the Intertropical Convergence Zone moves north (up to 4°), bringing precipitation to more northern latitudes [*Wilcox et al.*, 2010]. Another important implication of the presence of mineral dust in the atmosphere is the modulation of the Atlantic hurricane genesis and intensity [*Evan et al.*, 2006; *Sun et al.*, 2008]. A stronger westward penetration of the dust-carrying SAL allows for dryer conditions in the western Atlantic region, which are adverse to the development of tropical cyclones.

The amount of mineral dust aerosol in the atmosphere has been quantified using in situ data but mainly with the help of radiometer measurements onboard satellites. *Foltz and McPhaden* [2008a] have shown that 35% of the interannual variability of the North Atlantic summer SST can be explained by the variability of atmospheric dust load. Furthermore, the negative trend in North Atlantic dust content over the period 1980–2006, assessed by the aerosol optical depth (AOD) in the tropical region, was correlated with a corresponding positive trend in SST measured in the tropical Atlantic [*Foltz and McPhaden*, 2008b; *Evan et al.*, 2009]. The trend is probably part of multidecadal-scale variability of the North Atlantic, which was recently suggested to be related to African dust [*Wang et al.*, 2012; *Evan et al.*, 2012] using an extended reconstructed data set of mineral dust AOD.

At interannual-to-interdecadal time scales, the ocean surface temperatures are known to force climate variability over Africa and in particular the Sahel rainfall and, therefore, the deposition of desert dust [*Prospero and Lamb*, 2003]. Consequently, a significant correlation was found between dust deposition over the Atlantic and both the tropical Atlantic SST and the precipitation over West Africa. From changes in land use, *Mulitza et al*. [2010] additionally propose anthropogenic influences on the dust emissions from the Sahel over the past 200 years. A close relation between Saharan dust and Atlantic SSTs was also found in coupled climate models [*Mahowald et al*., 2011; *Yue et al*., 2011]. Allowing for dust-climate feedbacks, the climate response to aerosols is that of a net cooling, since the radiative-induced SST cooling brought about by the dust is accompanied by a decrease in precipitation, therefore decreasing the deposition of dust, which then remains in the atmosphere reinforcing the scattering of radiation [*Yue et al*., 2011].

Changes of solar radiative transfer into the ocean due to the presence of aerosols can alter the forcing of the ocean circulation. The dust radiative forcing impact on the upper ocean heat budget can produce changes in the vertical stratification of the ocean leading to enhanced vertical mixing, which by itself can change the deep density structure and the geostrophic flow field. In addition, dust-induced cooling at the eastern side of the North Atlantic could, in principle, generate a significant basin-scale horizontal pressure gradient with subsequent changes in the velocity fields and further changes in meridional transport of heat and volume. Such a mechanism would be consistent with findings by *Köhl* [2005], who investigated the mechanisms which are capable of changing the strength of the Meridional Overturning Circulation (MOC) at midlatitudes in the North Atlantic.

While changes of density along the western margin of the North Atlantic are traditionally considered a primary cause for modifying the MOC, *Köhl* [2005] results suggest that density changes in the eastern side of the basin are another possible cause for altering the MOC. More recently, *Heimbach et al*. [2011] showed the meridional volume transport in the North Atlantic to be sensitive to temperatures at 222 m depth in the eastern North Atlantic region off Africa. In addition, *Chidichimo et al*. [2010] found that density fluctuations in the eastern North Atlantic at 26.5°N contribute ± 2 Sv rms to the MOC variability, while the overall Atlantic MOC variability is 4.8 Sv rms. Moreover, the authors suggest that the amplitude of the MOC seasonal cycle is dominated by the one in the eastern boundary.

In this work, we investigate to what extent cooling induced by the presence of seasonally varying dust outbreaks can be another mechanism, besides wind stress curl and wind-induced upwelling, capable of changing basin-wide density gradients and thus the strength of the MOC and associated Meridional Heat Transport (MHT). Specifically, our work entails an analysis of the amplitude and the temporal and spatial scales of the basin-scale ocean response to dust-outbreak induced density changes in the subtropical eastern North Atlantic. To this end, we analyze a set of three-dimensional ocean model simulations run over a period of 5 years. Our goals are to determine (1) changes in the basin-scale horizontal circulation due to an imposed perturbation in the eastern North Atlantic and (2) to quantify associated changes in the transport of mass and heat in a basin scale due to an enhanced east-west density gradient.

Our approach is to investigate the response of the ocean circulation to net shortwave flux anomalies arising from seasonally varying changes in atmospheric dust content over the eastern subtropical North Atlantic by analyzing differences between perturbed and unperturbed simulations with respect to several key quantities. To isolate the dust-induced effects from other existing dynamical signals and from model artifacts, we study the impact of dust in the circulation using differences between perturbed and unperturbed simulations. The perturbed runs incorporate the dust effects in the subtropical eastern North Atlantic via a reduction of the net shortwave fluxes used to force the model. The expected first-order impact of the reduced net shortwave forcing is a cooling of the ocean surface.

The aim of our idealized study is to address the transient response of the ocean to radiative forcing in the eastern boundary brought about by a reduction of the net shortwave fluxes due to an idealized seasonal cycle in Saharan dust. Because of this, no other dust effects—such as dust-induced longwave radiation warming—are considered as further elaborated below. Moreover, the present work is only interested in the immediate (up to 4–5 years) response of the Atlantic (overturning and gyre) circulation, which justifies the short model integration. A long integration toward equilibrium, although possible, would suffer from low-frequency responses of the ocean, which are not the interest here and would mask the immediate, directly

induced response. Our choice to study the transient response makes the present work complementary to the recent study by *Evan et al*. [2012], which addresses the ocean response to African dust on decadal time scales.

The remaining article is organized as follows. Section 2 explains the model experimental setup and the construction of the net shortwave heat flux perturbation. In section 3, we investigate sea surface temperature and sea surface height differences between the perturbed and unperturbed model runs. Section 4 analyzes the vertical structure of the response and section 5 presents the associated anomalies in the horizontal gyre and meridional overturning circulations. The linearity of the ocean response is investigated in section 6 and the impact on the meridional heat transport is addressed in section 7. We conclude with a discussion and final remarks (section 8).

2. Methodology

Our study uses the MIT general circulation model [*Marshall et al*., 1997] to simulate the North Atlantic Ocean circulation forced response. The model configuration consists of a 1° horizontal resolution model, intended to only address the large-scale linear response of the ocean. The simulated Atlantic Ocean domain spans from 30°S to 65°N and includes the Mediterranean Sea. The open southern and northern lateral boundaries are forced with data from a global ocean state estimate using an adjoint data assimilation version of the MITgcm at 1° resolution (ECCO iteration 69). In the vertical, 50 levels are used with resolutions varying from 10 m in the upper layers to 500 m in the deepest layer. Background coefficients of vertical diffusivity and viscosity are set to 1×10^{-5} m^2 s^{-1} and 1×10^{-4} m^2 s^{-1}, respectively. The background coefficient of horizontal diffusivity is 100 m^2 s^{-1} and for viscosity it varies with the grid scale, ranging from 3×10^3 m^2 s^{-1} to 12×10^3 m^2 s^{-1}.

The model is initialized from rest with the WOA2001 annual-mean temperature and salinity; it was run subsequently twice for a period of 5 years, each time forced by the 1992–1996 daily fluxes of heat and freshwater and 12 h momentum fluxes from the NCEP RA1 reanalysis [*Kalnay et al*., 1996]. To prevent the model from drifting, a relaxation of surface temperature and salinity to the WOA2001 monthly climatology [*Conkright et al*., 2002] was used during the spin-up. Since the temperature relaxation would have the effect of suppressing the perturbation in the shortwave radiation that we want to impose, the fluxes resulting from the relaxation of surface temperature and salinity were stored and in a second step, net heat and freshwater fluxes were constructed that included the contribution of relaxation. Finally, the configuration is rerun for the second 5 years, but now only forced by the diagnosed, relaxation-corrected heat, freshwater and momentum fluxes. The resulting integration constitutes our unperturbed reference simulation.

In order to show the realism of the reference simulation, Figure 1 shows the Atlantic barotropic (Figure 1a) and overturning (Figure 1b) stream functions calculated for the unperturbed run and averaged over the entire 5 year period. Similarly to other coarse-resolution models, our simulation produces a time-mean horizontal gyre with extrema of about 50 Sv and 30 Sv in the subtropical and subpolar gyres, respectively, and a maximum MOC of about 18 Sv at 40°N (Figure 1b). A maximum time-mean MHT of 1 PW is achieved between 15°N and 30°N (thick solid line in Figure 1c), which agrees with the location and magnitude obtained by *Marotzke et al*. [1999]. The largest contributor for the MHT in the North Atlantic until about 45°N is the overturning component (thin solid line in Figure 1c). Northward from there it decays and the gyre component becomes, as also shown in *Hall and Bryden* [1982] and *Bryden and Imawaki* [2001], more important (thin dashed line in Figure 1c). Both the mean Atlantic MOC and MHT quantities of the control run are, therefore, in good agreement with respective estimates based on in situ observations, reinforcing the good performance of the model and its suitability to study the large-scale impact of the dust-induced cooling.

Along the northern African coast, the mean net shortwave flux distribution from the NCEP reanalysis shows a region of large net heating (Figure 2a) due to predominantly clear sky conditions in the North African upwelling region. Because no radiation reduction resulting from aerosols is incorporated in the NCEP reanalysis, a strong bias in the shown shortwave distribution can be assumed. The dust effect is incorporated here as negative shortwave flux anomalies added to the NCEP shortwave heat fluxes over the eastern subtropical Atlantic.

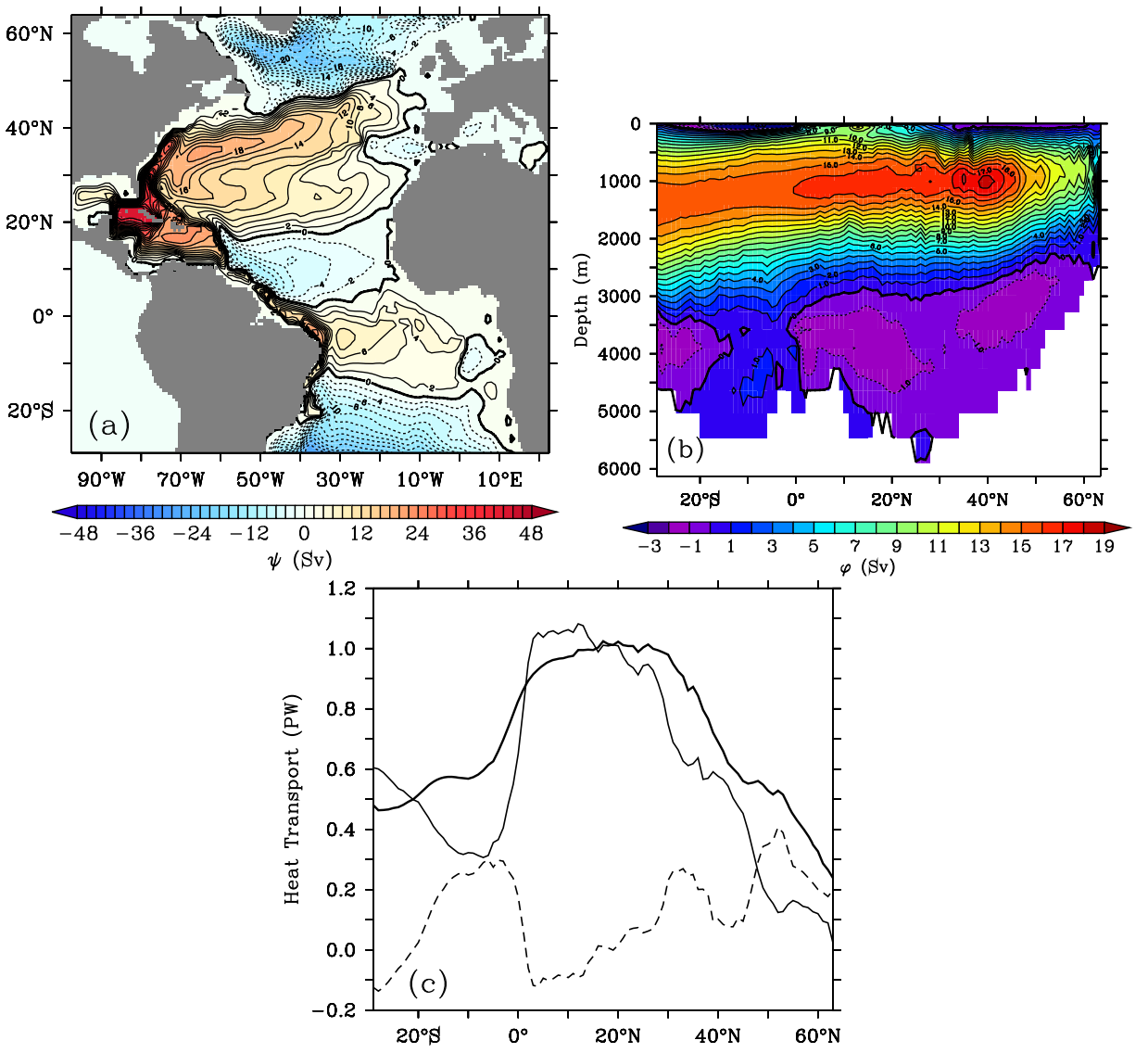

Figure 1. Time-averaged (a) barotropic ψ and (b) overturning ϕ stream functions from the unperturbed model experiment (in Sv). Positive values correspond to clockwise circulation. (c) Corresponding time-averaged total (thick) meridional heat transport (in PW) split into overturning (thin) and gyre (dashed) components.

A set of idealized net shortwave heat flux perturbations, $\tilde{Q}_{sw}$, are constructed by using a spatial pattern **L(x, y)** and a temporal pattern **T(t)** as follows:

$$\tilde{Q}_{sw}(x,y,t)=Q_{sw}(x,y,t)(1-a\ \mathbf{L}(x,y)\mathbf{T}(t)), \tag{1}$$

where Q_{sw} is the net shortwave heat flux available from the unperturbed run and a is a multiplying factor that controls the sign and amplitude of the perturbation. The spatial and temporal patterns, **L** and **T**, are nondimensional and allow the control of position and frequency of the perturbation. The spatial pattern **L** is constructed using the June/July/August average of aerosol optical depth (AOD) product from the MODIS sensor (Figure 2b) and is made nondimensional by normalizing it with the maximum value close to the African coast. The bias in the NCEP reanalysis supports the choice of our imposed perturbation pattern (Figure 3a), which is only defined (and therefore the perturbation only applied) in the high AOD area adjacent to the African coast.

Using different perturbations of the shortwave irradiance, several experiments were performed, as detailed in Table 1. The various experiments offer a range of possible ocean response magnitudes and also serve to

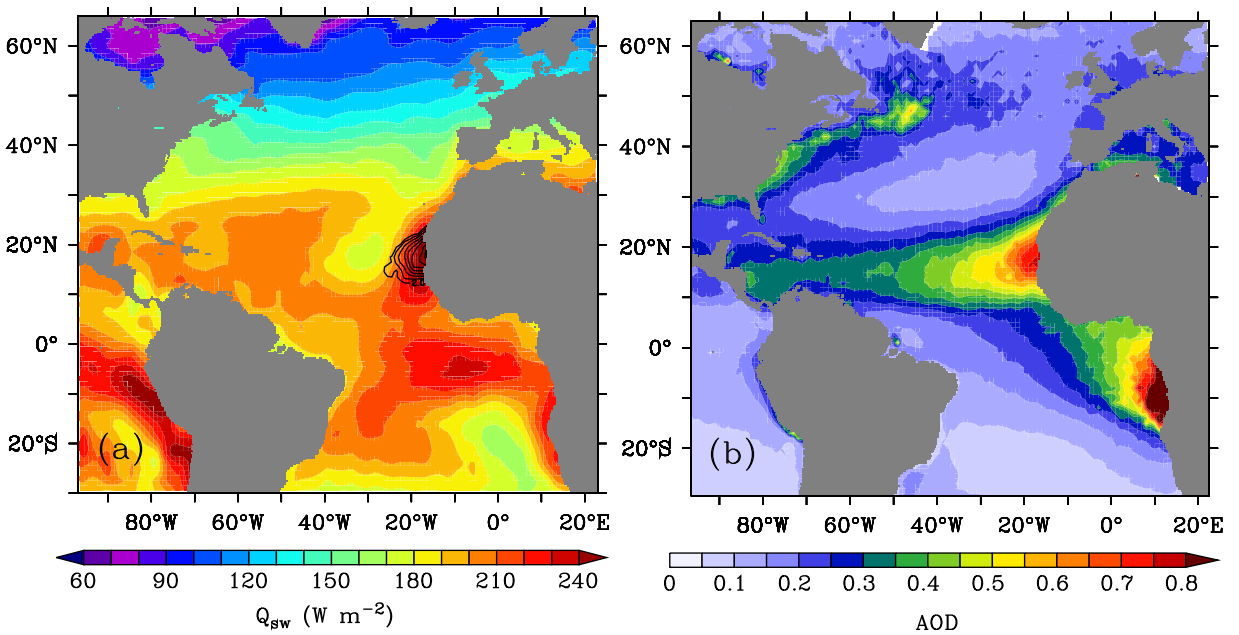

Figure 2. (a) Average net shortwave heat flux in the model domain (color shading, positive values correspond to ocean heating) and average perturbation (black contours, values vary from 0 to 17 W m^{-2}). (b) Summer (JJA) average Aerosol Optical Depth (nondimensional) in the North Atlantic from the 2000 to 2006 MODIS sensor data at 380 nm.

test the linearity of the resulting ocean response. In a first experiment (termed SINE), the temporal pattern **T** is a time series featuring a sinusoid with annual period (black curve in Figure 3b) and $a = 0.125$. In a second experiment (termed DOUBLE), the idealized wave (and thus the perturbation) has twice the amplitude (case $a = 0.25$) and in a third experiment (termed HEAT) its sign is reversed (case $a = -0.25$), i.e., the net shortwave heat flux is increased instead of decreased. In a fourth experiment (termed AOD), the time series is the aerosol radiative forcing (ARF = *fe*.AOD) derived from the actual 2000–2006 380 nm MODIS AOD values averaged in the area where the spatial pattern is defined (blue curve in Figure 3b) multiplied by the forcing efficiency (*fe*) computed in *Martínez Avellaneda et al*. [2010]. The above-idealized experiments focus therefore a seasonal perturbation of the net shortwave heat fluxes. See Table 1 for a summary of the amplitude of the net shortwave heat flux reduction close to the coast resulting from each experiment.

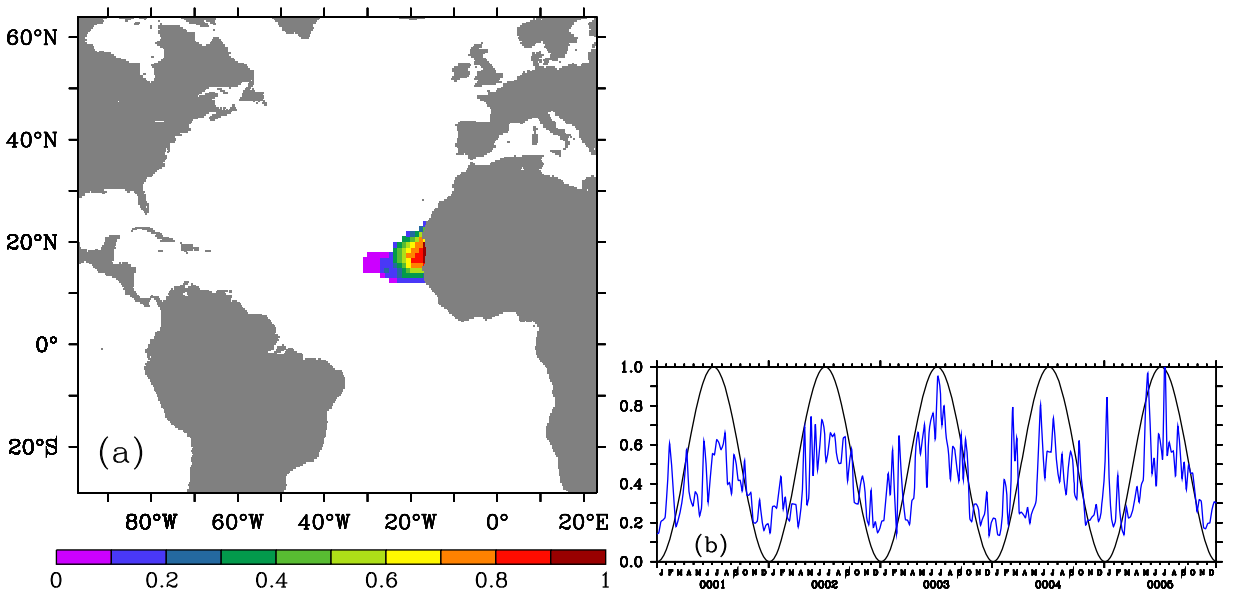

Figure 3. (a) Spatial and (b) temporal patterns of the idealized perturbation imposed to the net shortwave heat flux.

Table 1. Mean and Maximum Net Shortwave Heat Flux Reduction in the Perturbation Area Near the African Coast (16.5°W; 15°N)[a]

Experiment	Annual-Mean Reduction ($W m^{-2}$ and %)	Summer Maximum Reduction ($W m^{-2}$ and %)
SINE	−17 (7%)	−39 (13%)
DOUBLE	−34 (14%)	−78 (26%)
HEAT	+34 (14%)	+78 (26%)
AOD	−28 (11%)	−75 (25%)

[a]A positive sign in the heat flux changes corresponds to an increase.

As pointed out in *Miller and Tegen* [1998], the relatively strong radiative cooling at the surface contrasts with just a small net cooling at the top of the atmosphere (TOA), since the upward longwave radiation coming from the surface effectively warms the dust layer, therefore balancing the surface cooling. Some authors only reported values for the net radiative impact of Saharan mineral dust at the TOA [e.g., *Zhang et al*., 2005; *Christopher and Jones*, 2007]. These values are, however, not useful for guiding our idealized experiments, in which an estimate of the surface (shortwave + longwave) net cooling is needed to force the direct ocean response.

Miller and Tegen [1998, Figure 1] estimated the surface net radiation by mineral aerosols to be up to −15 W m^{-2} off West Africa. *Liu et al*. [2003] also point out to a value around −15 W m^{-2} for the diurnally averaged shortwave radiative forcing due to Saharan dust aerosol. During single dust outbreaks, *Myhre et al*. [2003, Figure 10] reported values of daily averaged radiative dust impact of up to −50 W m^{-2} in the same region. Furthermore, the magnitude of the longwave contribution was estimated to be 6–7 times weaker than the shortwave contribution. *Li et al*. [2004] estimated the surface aerosol forcing efficiency to vary between −65 W m^{-2} AOD^{-1} during the Saharan high-dust season (JJA) and −81 W m^{-2} AOD^{-1} during the low-dust season (NDJ). Assuming mean values of AOD for those seasons from *Zhu et al*. [2007], these forcing efficiencies would roughly translate into radiative reductions between −50 and −25 W m^{-2}. *Yoon et al*. [2005] present surface aerosol direct radiative forcing values at Cape Verde (off West Africa) ranging from winter to summer between −15 and −35 W m^{-2}.

Shortwave dust forcing values ranging from −45 W m^{-2} at the African coast to −15 W m^{-2} further offshore were computed by *Zhu et al*. [2007, Figure 9] for the JJA season. The estimated longwave contribution from dust (opposing the shortwave cooling) amounted to 40% of that from the shortwave radiation. Averaged over the whole area affected by dust off the African coast, the net surface shortwave plus longwave radiative forcing by dust was estimated for clear-sky conditions to be about −14 W m^{-2}. Finally, *Yoshioka et al*. [2007, Figure 2] arrived to net surface forcing values amounting to −13 W m^{-2} off the African coast. Their estimate of the shortwave cooling pointed to values smaller than −25 W m^{-2}; the opposing collocated longwave warming was in the range 3–10 W m^{-2}.

We note that, while experiment SINE in the present work features a reduction of −17 W m^{-2} in the forcing region, which is close to the observational [*Miller and Tegen*, 1998; *Liu et al*., 2003] and model estimates [*Yoshioka et al*., 2007] given above, experiment DOUBLE explores the high-end side of the estimates given in the literature [*Myhre et al*., 2003; *Li et al*., 2004; *Yoon et al*., 2005; *Zhu et al*., 2007].

In addition to the shortwave radiation-induced forcing incorporated in the simulations, the dust should account for other effects, such as (1) the already mentioned enhanced longwave radiation from dust-clouds thermal emissions [*Zhu et al*., 2007; *Evan et al*., 2009]; (2) changes due to dust-induced fertilization in the ocean; (3) enhanced turbidity due to dust deposition and further sinking; and (4) changes in the vertical profile of absorption of light due to (2) and (3). Although we are aware that some of the above-mentioned dust-induced changes in the system might be equally important as the shortwave heat flux forcing, an experiment that includes all the contributions was beyond the scope of this paper, which is intended as a process study, rather than a prediction of the real forced response. Therefore, in this work it is assumed that the first-order impact is on the net shortwave fluxes and therefore only this quantity was perturbed. The magnitude of the perturbation in experiment SINE is supposed to account for the missing longwave contribution.

Since the use of prescribed fluxes does not allow for a mechanism enabling the surface SST anomalies to be damped by air-sea interaction and, therefore, a potential exaggeration of the amplitude of the ocean response exists, we performed an additional set of experiments in which the SST of the perturbed SINE run was relaxed (restored) toward the SST from the unperturbed run. Since finding only one relaxation time scale, to be used throughout the whole domain and having a physical meaning, is difficult, a range of relaxation time scales (from 365 days to 30 days) were used. As expected, over the short period considered here,

the relaxation experiments gave patterns of ocean response very similar to the ones obtained from prescribed surface fluxes. The magnitude of response decreased according to an increase in damping (decrease of relaxation time scale). From all relaxation experiments, those that gave an SST response magnitude around 0.5°C, a value established from observations [*Evan et al*., 2009; *Martínez Avellaneda et al*., 2010] and other model studies [*Yoshioka et al*., 2007], used relaxation scales in the range 90 d–180 d. So, results from these two experiments (90 d and 180 d) will be shown farther ahead to give an idea of the uncertainty in our model estimates.

3. Sea Surface Temperature and Height Response

The response of the model sea surface temperature (SST) and sea surface height (SSH) to the shortwave anomalies is analyzed here as the difference between the perturbed and unperturbed runs; henceforth, those differences will be termed ΔSST and ΔSSH. In this context, the temperature of the first model vertical level (at 5 m) is taken as representative of the SST. Moreover, we are also interested in steric changes of SSH brought about by our imposed ocean cooling (warming in case HEAT). Since the MITgcm uses the Boussinesq approximation, it conserves total volume and so, mass gain (loss) from cooling (warming) will be compensated by a large-scale redistribution of mass in the basin [*Greatbatch*, 1994; *Ponte*, 1999], a signal leading to bottom pressure changes. To recover steric SSH signals, the simulated SSH is corrected for bottom pressure changes.

Experiment SINE results in an annual-mean reduction in the net shortwave heat flux of about 7% (17 W m^{-2}) near Africa, gradually vanishing away from the coast (black contours in Figure 2a). The summer maximum reduction amounts to 39 W m^{-2} (i.e., 13% of the summer maximum value). The associated yearly averages of ΔSST and ΔSSH are shown in the left and right columns of Figure 4, respectively. As can be seen from the figure, the first-order impact of the cooling is a reduction of SST by about 0.5°C and a depression in SSH by about 0.5 cm after 1 year, when the anomalies still have the shape of the shortwave flux perturbation spatial pattern and are confined to the region adjacent to the African coast. While the net shortwave reduction in the SINE experiment is within the limits assumed for the real dust-induced forcing, we recall here that our experiments merely serve the purpose of identifying the perturbed response spatial and temporal patterns of the Atlantic circulation, rather than targeting quantitative conclusion.

During the subsequent 2 years of integration, anomalies are being advected toward the west to the point that a—albeit weak—signal in ΔSSH reaches the Antilles by year 3. A pathline integration of the two-dimensional top 500 m average flow field is shown in Figure 4b, illustrating that the main circulation pattern of the upper Atlantic Ocean indeed determines the spread of the anomaly. We note, however, that the surface temperature signal is more confined to the eastern basin as compared to ΔSSH, which shows a more zonal propagation.

During the following years 4 and 5, the ΔSST and ΔSSH signals completely reach the western margin at depth. Subsequently, both fields begin to show small-scale features downstream of the Gulf Stream along the North Atlantic Current, revealing that once the strong current systems are impacted (like the Florida Current and the Gulf Stream), slightly different eddy signals are generated leading to small-scale anomalies further downstream along the North Atlantic Current; this holds in particular off the Grand Banks of Newfoundland. However, the largest amplitude anomalies remain (absolute values below 2°C and 2 cm), as expected, in the direct reach of the forcing anomalies off the western African coast.

We conclude from this experiment that a response of the basin-wise subtropical Atlantic circulation to buoyancy perturbations generated near the eastern side of the North Atlantic is to be expected. As will become more clear in section 4, a general difference between the SST and SSH response is the confinement of the temperature anomaly to the eastern side and the ocean interior, while SSH anomalies, representing vertically integrated density anomalies as well as changes in the circulation, can be traced across the entire basin. Time scales for the propagation of the SST and SSH anomalies are given in Figure 5. The figures show the time (in years) taken for the local perturbation to achieve 1% (Figures 5a and 5b) and 10% (Figures 5c and 5d) of its absolute maximum value, therefore illustrating the fastest propagation pathways. Seen in the figure is a coastally trapped signal propagating northward along the eastern boundary downstream of the forced region. The feature is consistent with a coastal Kelvin wave and shows a decay time scale up to 1 year, a period required to reach the subpolar basin.

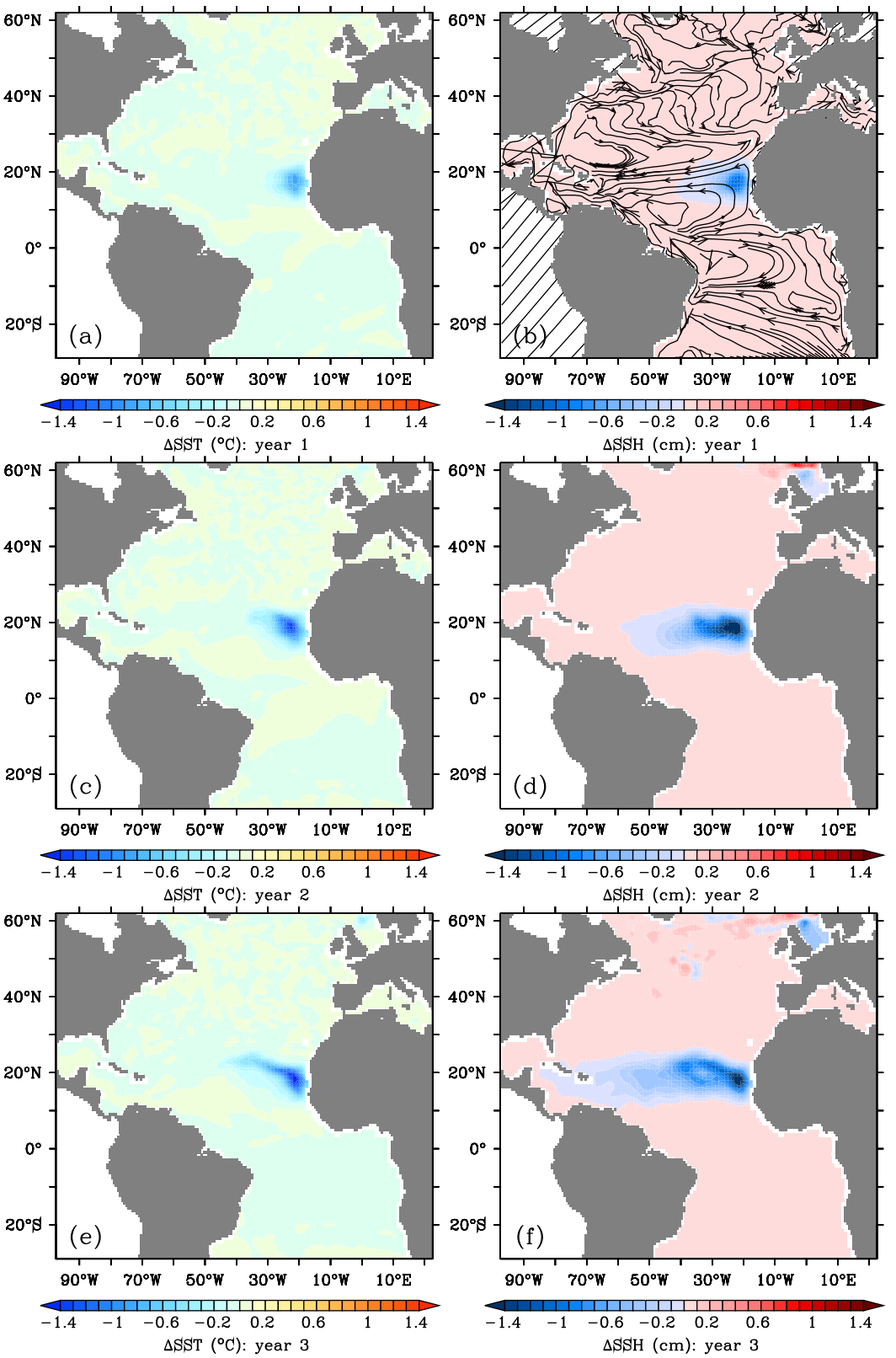

Figure 4. Anomaly (relative to the unperturbed experiment) of (left) Sea Surface Temperature (°C) and (right) Sea Surface Height (cm) for the experiment with a pure seasonal cycle in the perturbation to the net shortwave heat flux (SINE). Flow lines in (b) depict the model average top 500 m ocean circulation.

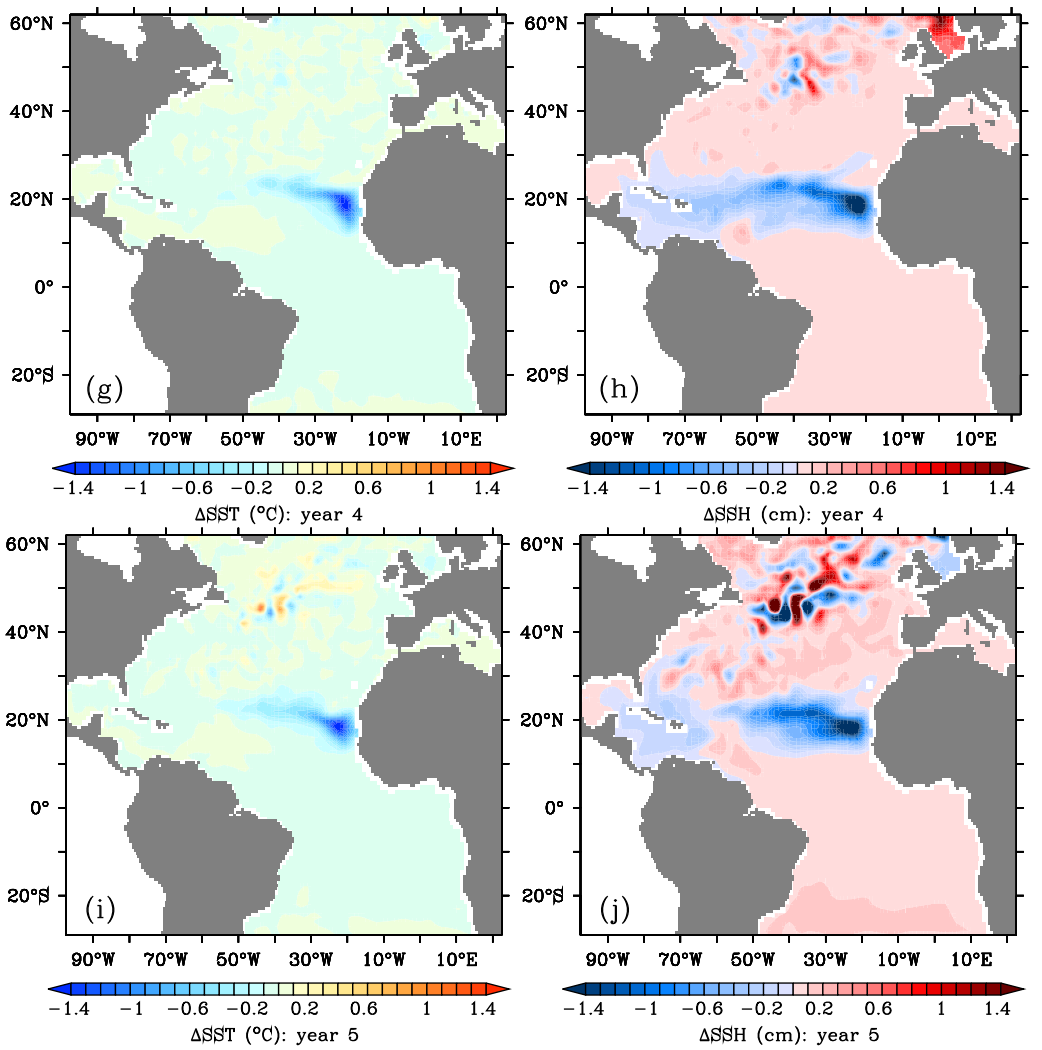

Figure 4. (continued)

With the course of the integration, the anomalies in the north are included in the subpolar gyre circulation, there implicating the dense-water formation. This, in turn, potentially impacts the northern part of the Atlantic meridional overturning cell and so a response in overturning and heat transport can emerge due to signals in the north. However, this mechanism acts at time scales longer than the 5 year simulation time and the magnitude of response in heat transport during the 5 years is small.

4. Vertical Structure of Temperature Anomalies

To help understand the response of the temperature and density fields and the westward propagation of respective anomalies, it is instructive to analyze the vertical structure of those fields. Figure 6 shows an east-west section of temperature differences ΔT at 20°N averaged for each of the first 4 years of the SINE experiment. From the figure, it becomes obvious that the anomalous cold signal in ΔT, imposed by the shortwave perturbation on the eastern side, propagates toward the west while at the same time progressively deepens. We note that the strongest signal remains confined to the top 500 m and that, at the shown latitude, the signal seems to arrive at the western basin after only 4 years, while at the same time continuously deepening.

The southern limb of the subtropical gyre is well known for its role in the subduction of water masses. *Marshall et al.* [1993] have estimated subduction rates for the North Atlantic. From their estimates, a subduction

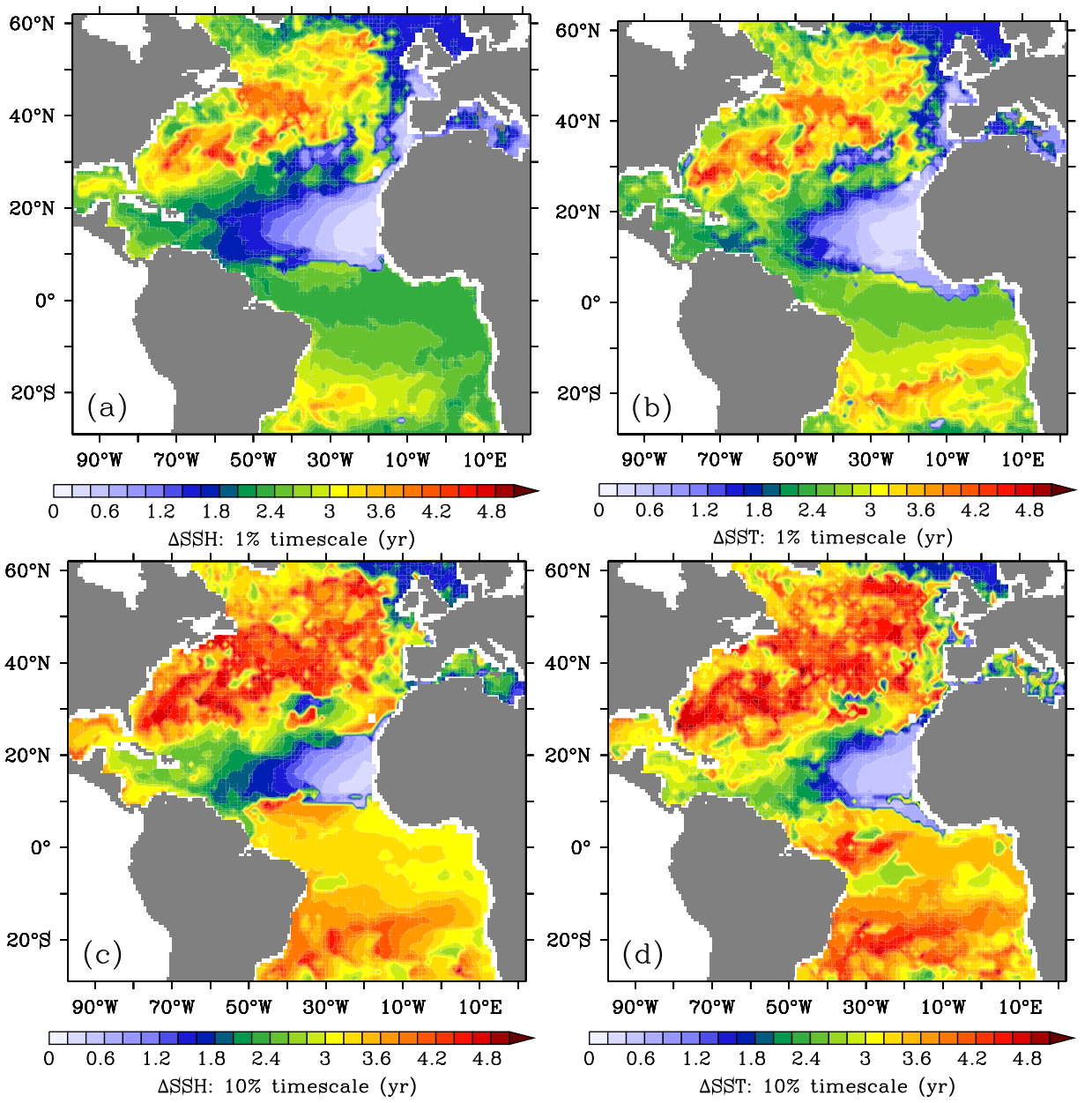

Figure 5. Elapsed time for the (a and c) Sea Surface Height and (b and d) Sea Surface Temperature perturbations to amount to (a and b) 1% and (c and d) 10% of its maximum magnitude (in years).

rate between 50 and 100 m/yr is to be found in the subtropical gyre. A subduction of that magnitude can indeed explain the deepening of the signal seen in Figure 6. On the other hand, the average background circulation in the perturbed area supports a westward advection of the anomalous signal (Figure 4b).

We can also trace the temperature anomaly to deepen toward the south as displayed in Figure 7, showing ΔT along 15°N, 20°N, and 25°N, averaged over year 5. It can be seen that north of the perturbation axis the anomalies are very superficial and the ΔT shows smaller amplitudes and less zonal extent. On the other hand, in the south, the anomaly is almost completely capped by a positive anomaly present at the surface. This is again indicative of the large-scale north-south subduction pattern in the southern part of the subtropical gyre.

From a comparison of Figure 8, showing the anomaly during year 5 at 50 m, 120 m, and 300 m depth, with Figure 4, showing year 5 ΔSST, it becomes obvious that the temperature anomaly in the central Atlantic

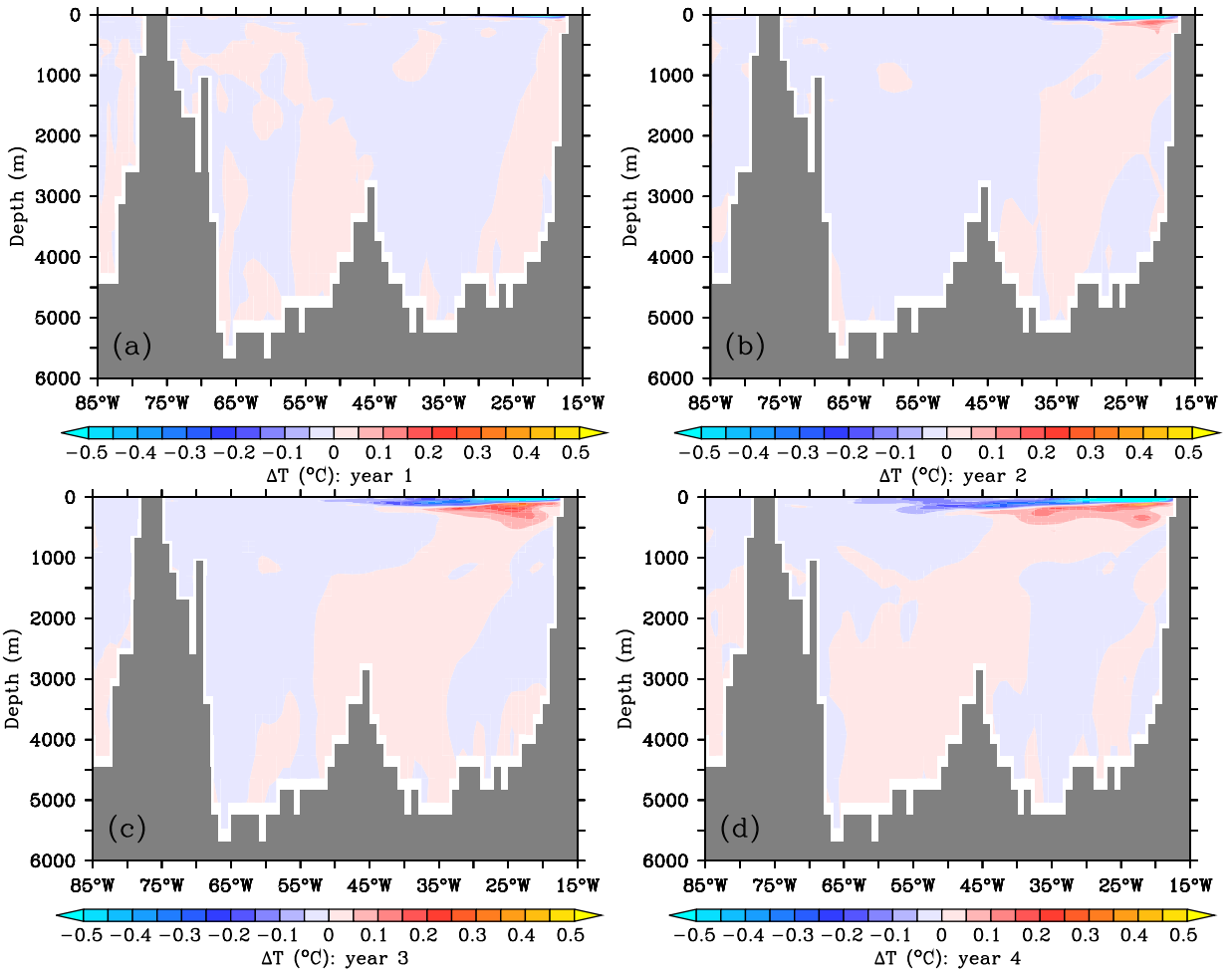

Figure 6. Vertical sections of ΔT (in °C) averaged at 20°N for integration years 1–4 (a–d) from experiment SINE with a pure seasonal cycle in the perturbation to the net shortwave heat flux.

resides at greater depth than the initial subduction depth and that the anomaly arrives to the Caribbean Sea deeper in the water column. At the same time, we see a positive temperature anomaly appearing underneath the cold SST anomaly at the eastern boundary (also seen in Figure 7b). The positive anomaly is seen to extend further to the west at 300 m depth (Figure 8c).

The presence of a positive ΔT beneath the cold anomaly in the eastern basin at 20°N results partly from deeper wintertime entrainment mixing under the forcing region due to a deepening (thickening) of the mixed layer. This is illustrated in Figure 9, showing the time evolution of ΔT in a location beneath the largest forcing. The positive anomalies emerge at about 80 m depth during winter. The potential density at that location is shown both for the unperturbed (black contours) and the SINE perturbation (red curves). The base of the winter mixed layer is some 20 m deeper in the perturbed case, which is a consequence of the extra cooling at the surface and consequent convective motions in the mixed layer. As was shown by *Martínez Avellaneda et al.* [2010], a mixed layer deepening is the expected 1-D response to the surface cooling. At the base of the mixed layer, cool water is mixed upward and warm water mixed downward in a turbulent entrainment process maintained by wind forcing (we recall that the experiments include realistic wind stress forcing from the atmospheric reanalysis). Once the mixed layer depth is deeper, the mixing process will occur deeper and the temperature difference to the control experiment will show a warming at depths where in the control run the mixed layer was not reaching. This signal immediately begins to be subducted and advected with the mean flow and therefore can be detected further west. So, subduction and advection are responsible for the deepening and westward spreading of the subsurface anomaly in the upper 500 m.

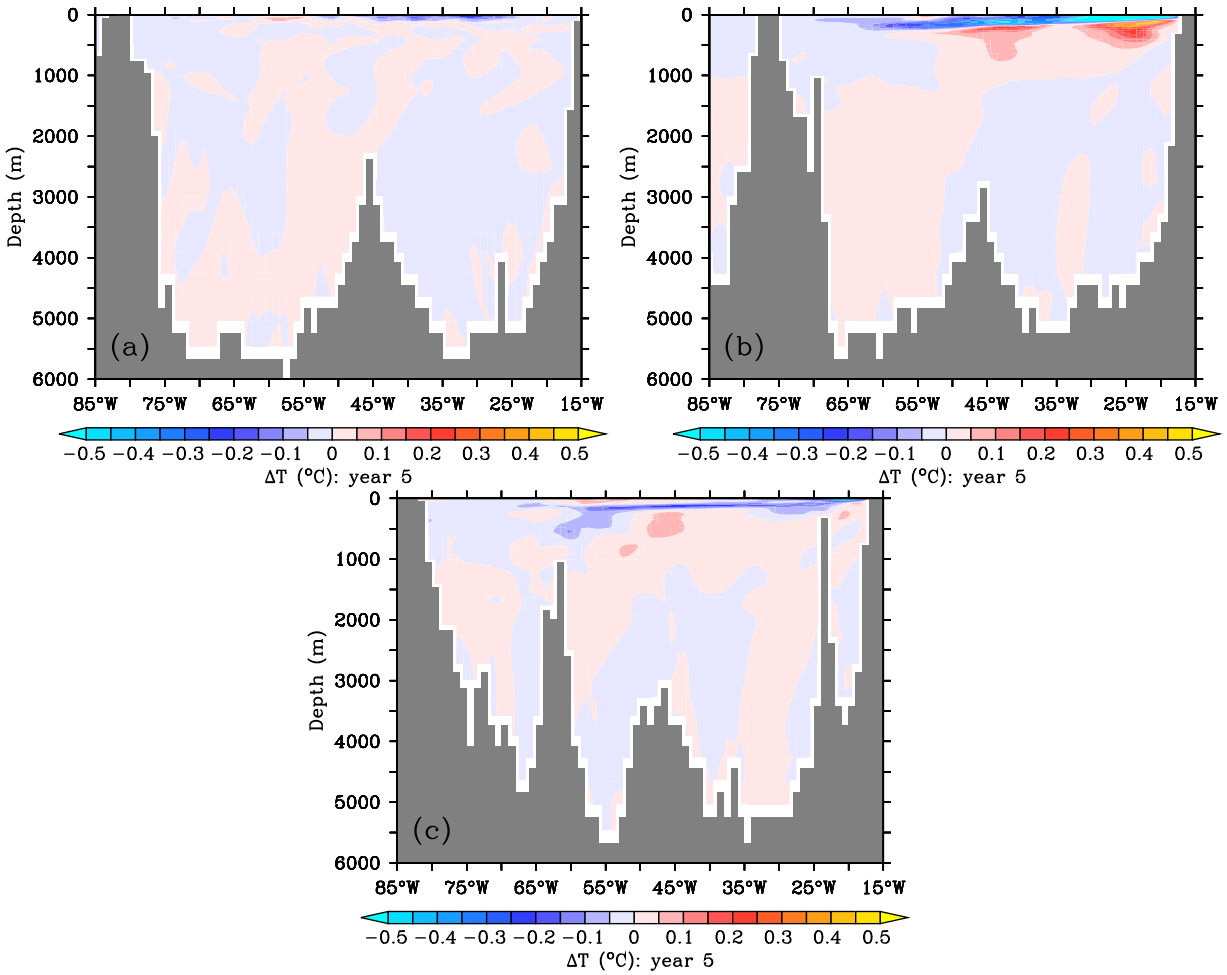

Figure 7. Vertical sections of ΔT (in °C) averaged at (a) 25°N, (b) 20°N, and (c) 15°N for integration year 5 of experiment SINE.

From Figure 6a, a second important aspect of the ocean temperature response becomes evident. It is related to the small-amplitude banded structure encompassing the whole water column. In fact, the SINE experiment (and all other surface cooling experiments) shows a deepening of the isotherms below the mixed layer (more visible in the layer 100–600 m). This heaving process is a consequence of a dynamic response of the ocean, as will be shown in section 5. This downlift of the isotherms might be coresponsible for the warm anomaly seen below the mixed layer cooling. Figure 6 also suggests that a low-frequency Rossby wave mode is excited, since some propagation can be appreciated in the course of time (see Figures 6 and 7b). Judging by the vertical pattern, it might correspond to an ocean baroclinic mode. *Köhl* [2005] studied the processes relevant for understanding the variability of the Atlantic MOC at 30°N and found that temperature anomalies generated in the eastern North Atlantic can indeed propagate as long Rossby waves and promote transport fluctuations in the western boundary.

In order to gain further insight into the behavior of the mixed layer under the cooling area, Figure 10 presents the complete local heat budget under the forcing region (16°W–28°W; 13°N–23°N; 0–90 m). The main result is that, locally, the heat import/export from the defined box (the ocean divergence) cannot be ignored and that the balance after about 1 year is established between the imposed surface heat flux anomaly and the anomalous ocean heat divergence (Figure 10a), with the heat content in this box reaching equilibrium (Figure 10b). Since there is a convergence (negative sign in the divergence term) of heat into the box, it can be shown that the anomalous signal comes mainly from the northern and western boundaries (Figure 10c). As will be shown ahead, the anomalous convergent heat is actually due to the westward export of cold water. Finally, accounting for missing feedbacks (associated with surface turbulent fluxes)

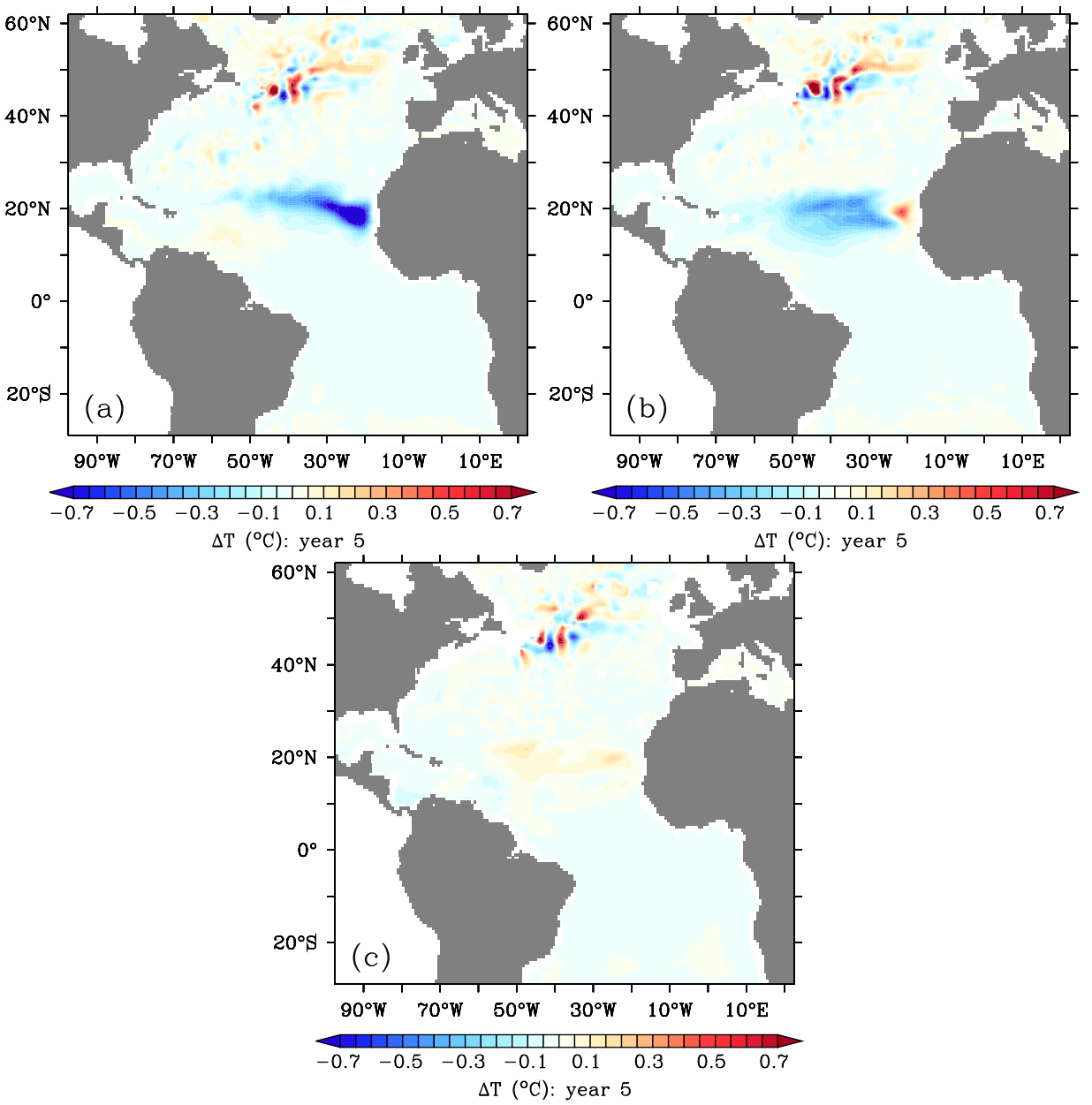

Figure 8. Horizontal maps of ΔT (in °C) averaged for integration year 5 of experiment SINE at (a) 50 m, (b) 120 m, and (c) 300 m.

through the use of surface damping (here the relaxation time scale of 90 d is used), the overall result does not change (Figure 10d), meaning that the heat convergence cannot be neglected and that the missing processes can at best be as large as the ocean counterpart of the heat divergence. In conclusion, heat advection cannot be neglected and contributes to the damping of the surface-imposed fluxes [*Foltz and McPhaden*, 2006]. The latter fact has consequences to the reliability of estimates of damping time scales obtained with simplistic models disregarding an ocean active role.

Anomalies of the vertically integrated heat content and of vertically integrated heat flux in the top 300 m are presented in Figure 11. They clearly show that the western subtropical basin response within the first 4 years is solely due to the advection of the cold anomaly by the mean flow, and/or perhaps also to westward Rossby wave propagation (as noted in Figure 6).

The average 0–300 m heat flux is directed primarily westward in our study region (Figure 11a), as part of the North Equatorial Current. The evolution of the heat content anomaly and the circulation change associated with

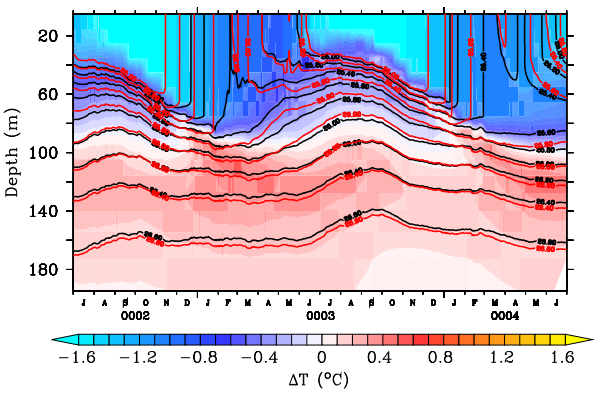

Figure 9. Depth-time evolution of ΔT (SINE experiment—colors) and potential density from unperturbed (black contours) and perturbed (SINE experiment—red contours) runs at the location of maximum surface forcing by net shortwave flux reduction.

it is shown in subsequent plots of Figure 11. Over the course of the first 4 years, the circulation changes occur in the tropical Atlantic between 5°N and 30°N. Soon a cyclonic circulation anomaly (about two orders of magnitude smaller than the mean) establishes around the negative heat content anomaly. The flux at about 15°N is to the east, which corresponds to the positive net heat flux into the area where the radiative anomaly is imposed, as seen in the heat balance of Figure 10c.

With the course of time, the cyclonic circulation extends to the west, in fact extending faster than the negative heat content anomaly. Already after 3 years, all the western boundary current systems are affected: a stronger North Brazil Current and a reduced Florida Current are seen (Figures 11c and 11d). This is hypothesized as being a result of fast westward propagating Rossby waves. After 4 years, the whole tropical region including the Caribbean Sea shows a cold anomaly, with the four strong cold pulses (four summers of anomalous radiative forcing) taking a somewhat northern path at about 20°N.

The southern part of the established anomalous circulation shows a heat flux toward the east. But what seems to be a supply of heat to the forcing region is solely a (slightly weaker) mean advection of cold water. The mean heat supply to the forcing region is still from the south along the African coast (Figure 11a), a region that does not show anomalies (Figures 11b–11d). So, what is seen as an anomalous heat advection

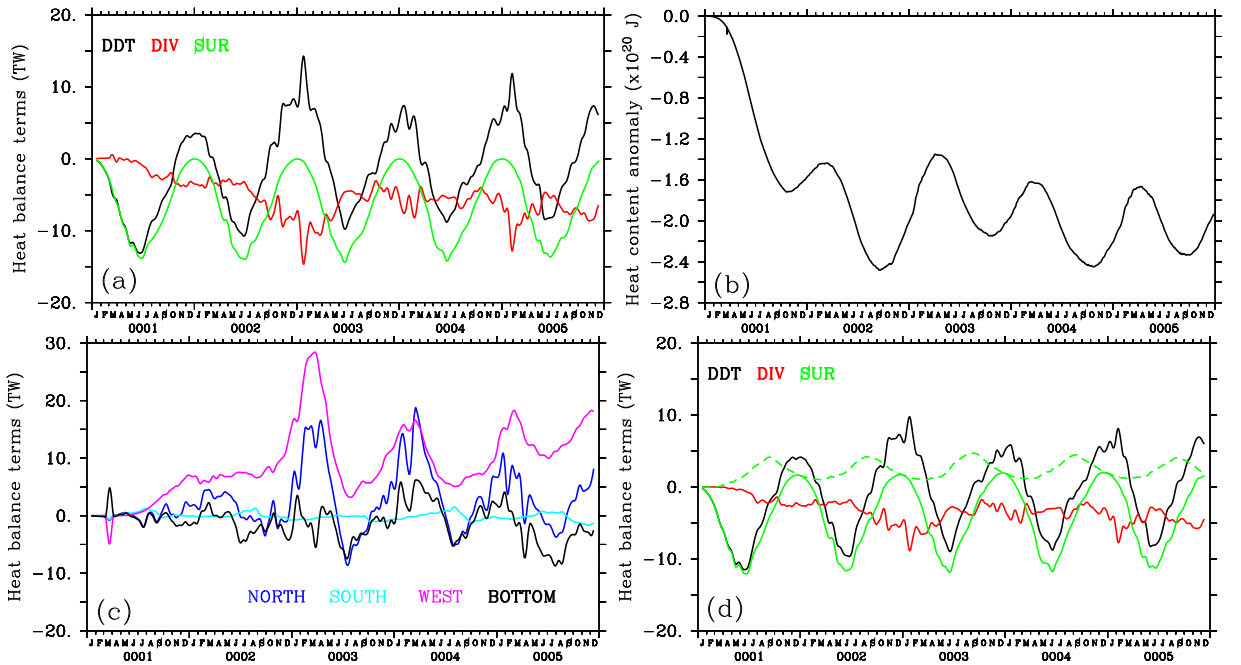

Figure 10. (a) Anomalies (perturbed minus unperturbed) of heat balance terms under the forcing region in the eastern boundary (from 16 to 28°W and 13 to 23°N) from experiment SINE: black—heat content change; red—horizontal heat divergence + advective and diffusive fluxes at depth of maximum mixed layer (90 m); green—surface heat flux. (b) Anomaly of the respective box-integrated local heat content. (c) Anomalies of the heat divergence terms: blue—northern boundary horizontal flux; cyan—southern boundary horizontal flux; magenta—western boundary horizontal flux; and black—vertical flux at 90 m + diffusion term. (d) Same as Figure 10a but for the experiment including a relaxation time scale of 90 days (the dashed green line corresponds to the contribution from the relaxation to the surface heat flux and the solid green line to the remaining part).

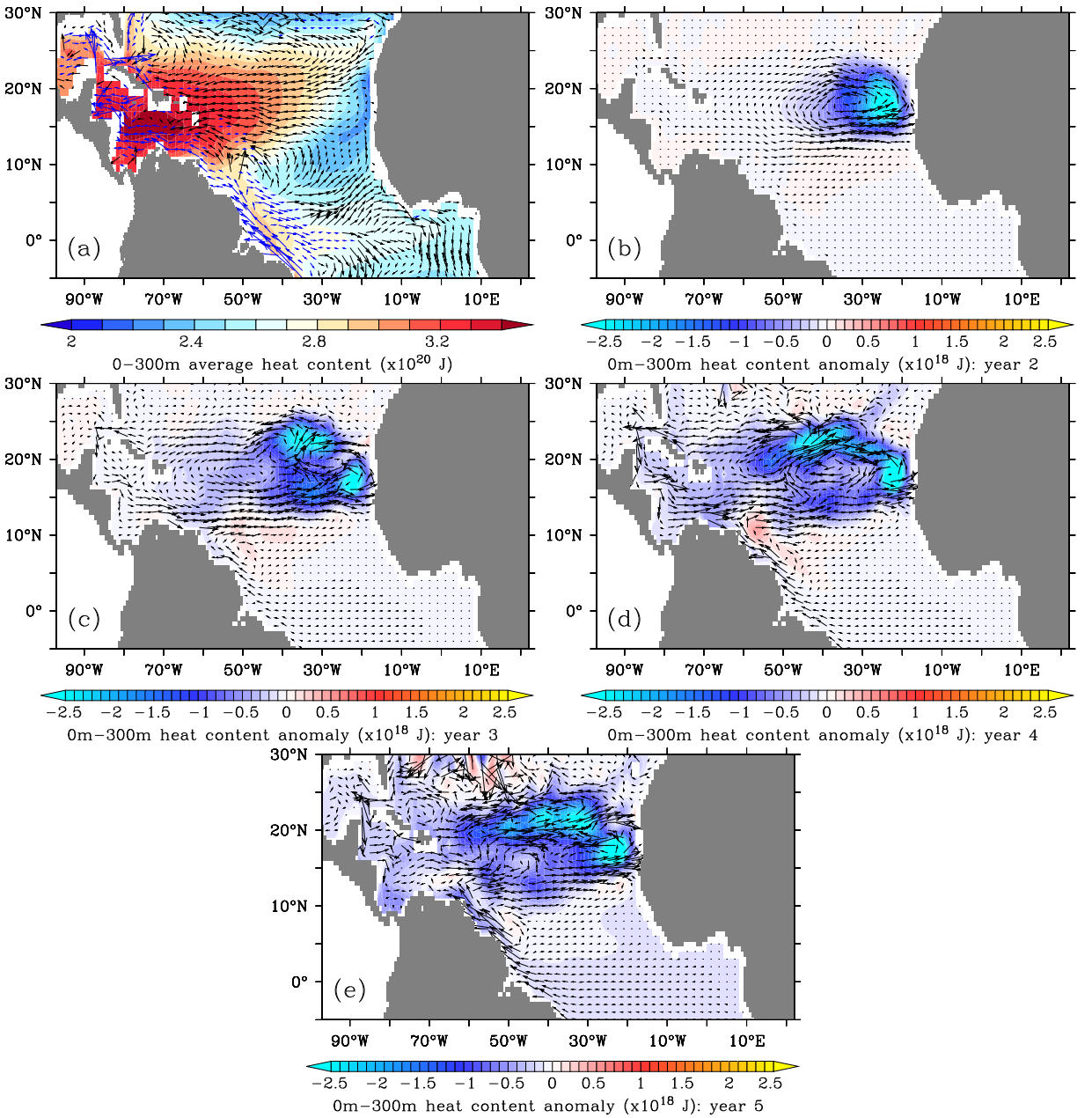

Figure 11. (a) Average 0–300 m vertically integrated heat content in the unperturbed experiment with the 0–300 m vertically integrated heat flux vectors superimposed. The corresponding annual anomalies (SINE experiment minus unperturbed run) are shown for years (b) 2, (c) 3, (d) 4, and (e) 5.

to the east feeding the area where the heat is being extracted by the atmosphere is only a result of the cold advection out of the forcing area.

The differences in density between the perturbed and the unperturbed runs during year 5 of experiment SINE (not shown) present positive values that at the surface reside in the eastern basin beneath the cooling forcing region and at 120 m are concentrated in the western Atlantic. This opens the possibility for horizontal east-west density gradients. Therefore, an important consequence of the cooling signal in the eastern basin is the possible change in the North Atlantic basin-wide density gradient, and thus to a change of the interior basin component of the Atlantic MOC (see section 5 for details).

To quantify the Atlantic basin-wide density gradient resulting in the perturbed experiments, Figures 12a and 12b display the differences in mean east-west horizontal density gradient ($\Delta(\rho_E - \rho_W)$) between the

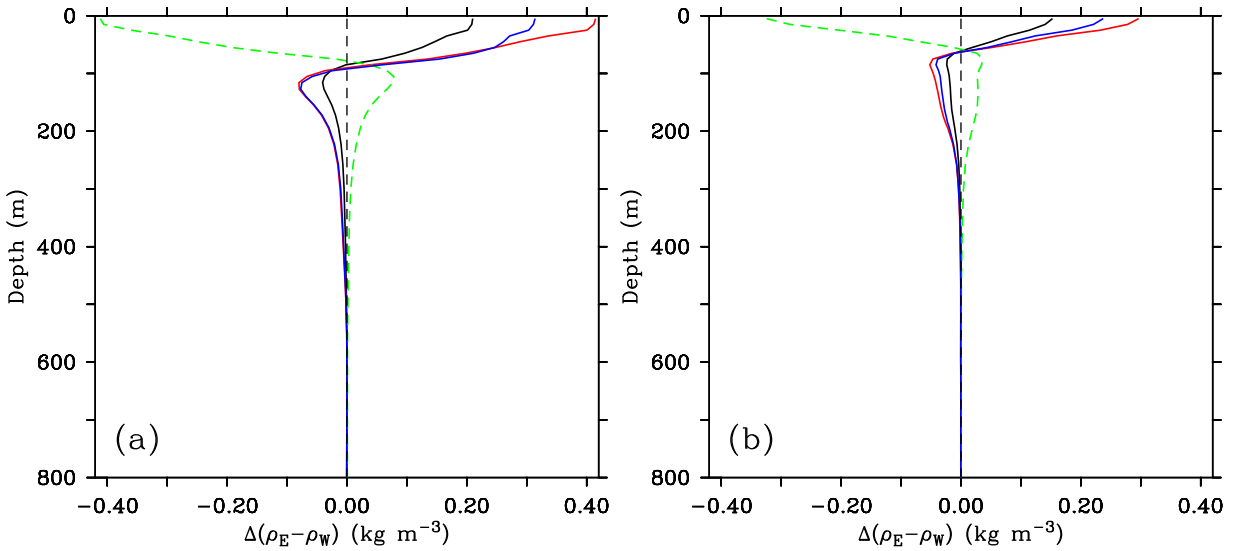

Figure 12. Vertical profile of the anomaly (relative to unperturbed experiment) in mean basin-wide east-west density difference at (a) 20°N and (b) 15°N for different experiments (see text): black—SINE; red—DOUBLE; green—HEAT; and blue—AOD.

four perturbed experiments and the unperturbed run at 20°N and 15°N, respectively. Under dust-induced cooling conditions (black, red, and blue curves) an increase in the horizontal density gradient can be observed, which is proportional to the forcing intensity. The signal is intensified in the top 300 m but slightly varies in reaching depth among the experiments. Stronger perturbations lead to stronger subduction of the density signals and to deeper-reaching density gradients. Below 90 m, the anomalies have a reverse sign, meaning that the horizontal density gradient reduces there. This reduction reaches up to 400 m at 20°N and only up to 300 m at 15°N. This negative anomaly will contribute to partially cancel the vertically integrated transport and therefore the impact on the MOC will not be as large as it would be expected from the top 100 m density gradients. In case a heating anomaly would result (experiment HEAT; green curves), the horizontal density gradients have slightly shallower differences to the unperturbed run, despite the forcing magnitude being the same as DOUBLE. This is due to the stabilizing nature of the anomaly and the less effective subduction of the positive density (light) anomalies in that case.

5. Atlantic Barotropic and Overturning Stream Function Anomalies

Differences between perturbed and unperturbed barotropic and overturning stream functions ($\Delta\psi$ and $\Delta\phi$, respectively) are shown in Figure 13 for each integration year of the SINE experiment. The barotropic stream function is a vertically integrated quantity, so it might reflect, at different locations, current structures intensified at different depths. The interpretation is, therefore, not straightforward. For instance, the barotropic circulation does not completely reflect the local cyclonic surface anomaly induced by the cooling near the African coast seen in Figure 11. This is due to a compensating effect originating from the deeper positive heat anomaly, which developed beneath the cooling (see section 4).

Figure 14 presents the anomalies of the 300–1000 m vertically integrated heat content and horizontal fluxes. It can be noticed that during year 2 an anticyclonic anomaly (Figure 14b) is already seen below the cyclonic anomaly associated with the surface cooling in the mixed layer (see Figure 11b). As a consequence, vertical compensation occurs and the net barotropic flow vanishes under the forcing region (Figure 13c). The anticyclonic circulation in deeper levels most probably causes of the deepening of the isopycnals below the mixed layer mentioned in section 4. It therefore reflects an indirect dynamic response of the ocean to the cooling, in this case leading to a small but important adiabatic change in the temperature structure below the mixed layer. In experiment HEAT, in which the surface was warmed by a positive shortwave flux anomaly, the reverse case occurs: an anticyclonic circulation is established around the anomalous warming pattern; in response, the deeper layers developed a cyclonic circulation anomaly and promoted an uplift of the isotherms, leading to a cool anomaly beneath the mixed layer.

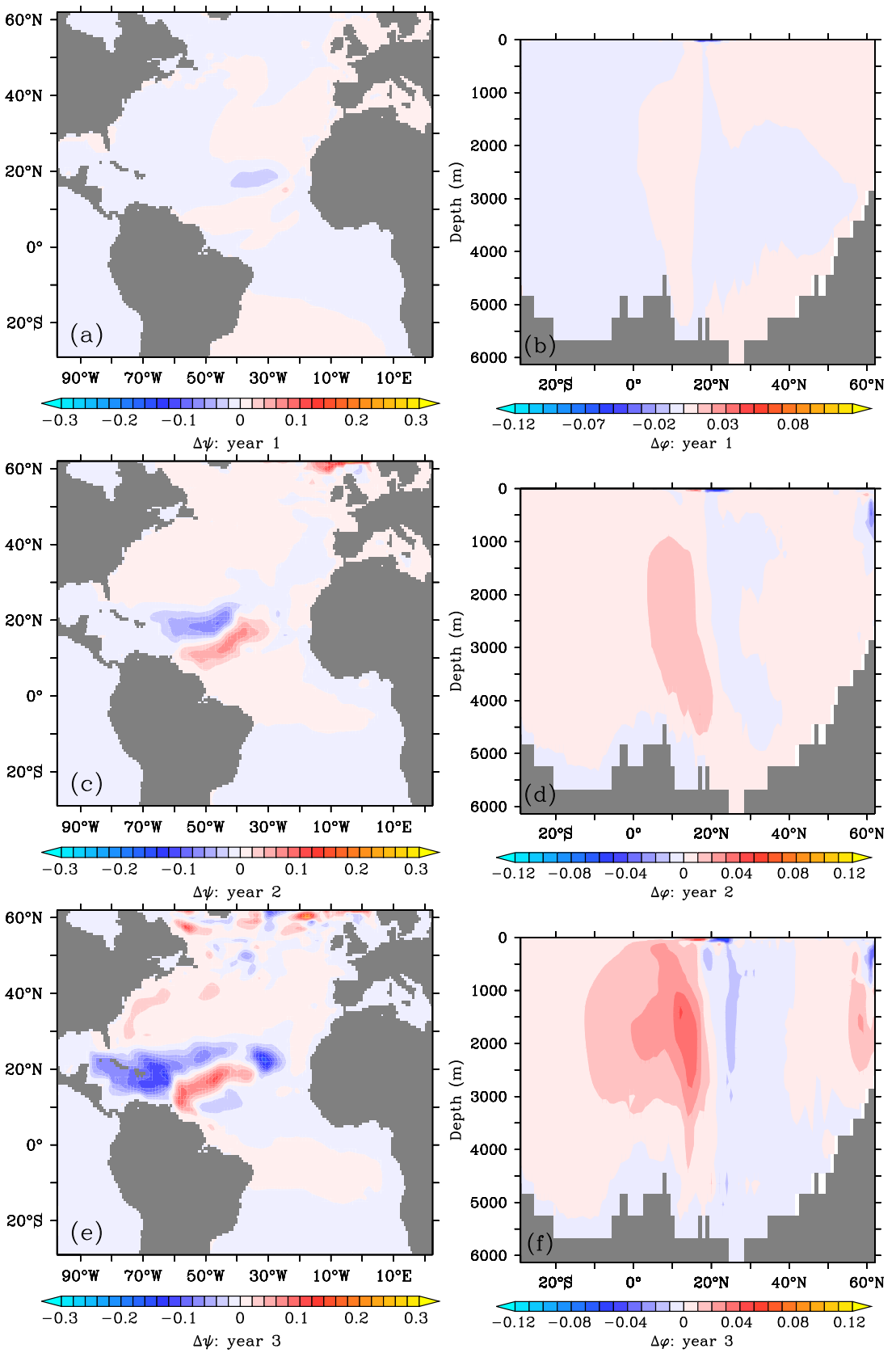

Figure 13. Anomaly (relative to the unperturbed experiment) in (left) barotropic stream function (Sv) and (right) meridional overturning stream function (Sv) from the SINE experiment.

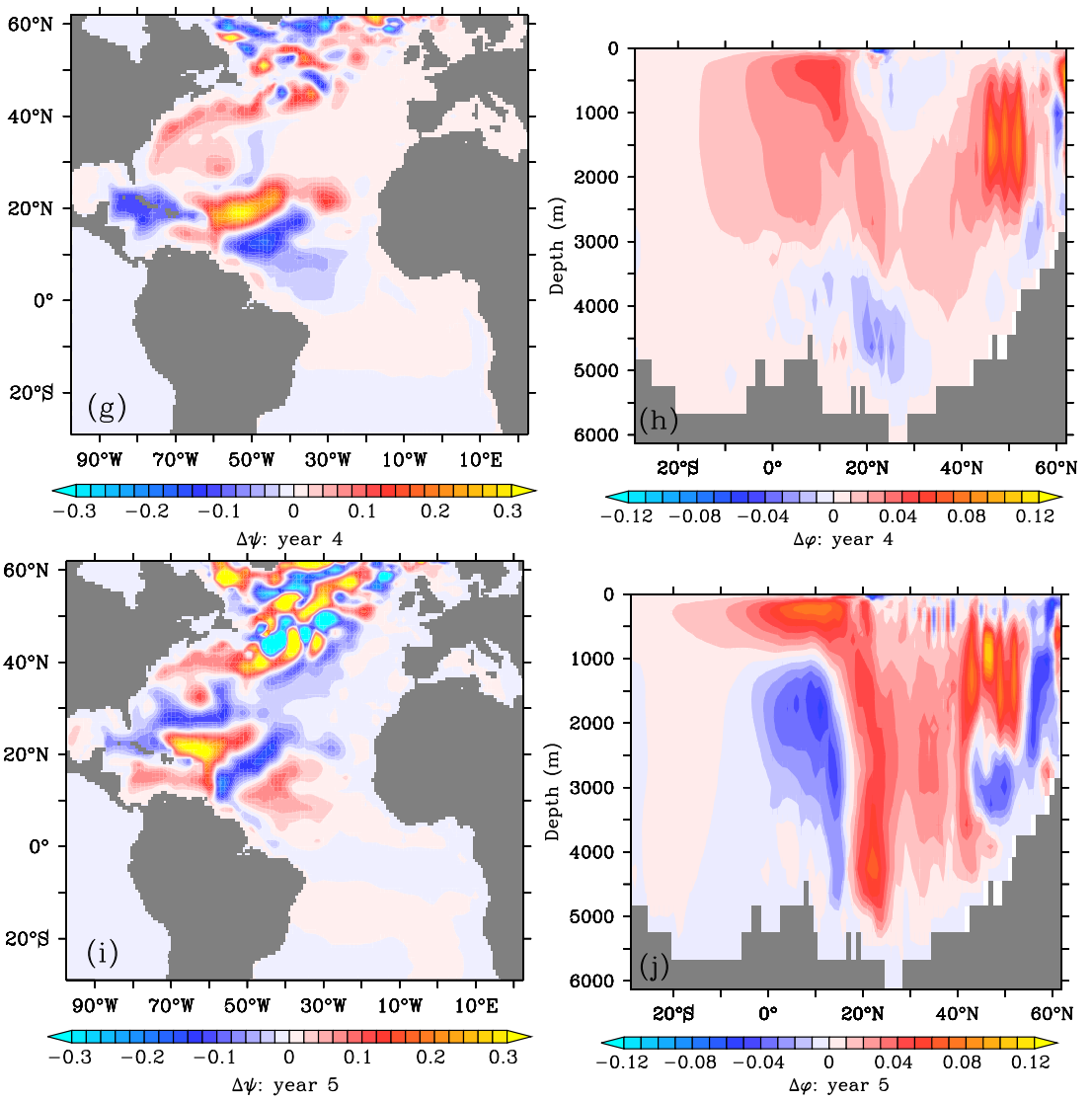

Figure 13. (continued)

The year 2 averaged $\Delta\psi$ in Figure 13 shows a clear dipolar pattern (negative anomaly in the north and positive in the south) extending in the northeast-southwest direction from roughly the Mid-Atlantic Ridge, a feature not noticeable either in ΔSST or ΔSSH. In fact, the positive part of this anomaly can only be explained by the deeper (1000–3000 m) transports, included in Figure 15.

By year 3, the barotropic flow in the Caribbean Sea presents a negative anomaly (transports decrease up to 0.15 Sv). This cyclonic anomaly was seen in the top 300 m (Figure 11c) and extends down to 1000 m depth (Figure 14c). North of 40°N small-scale features appear but are unrelated to the stream function anomalies in the tropical region. During year 4, the positive $\Delta\psi$ anomaly north of the South American continent (Figure 13g) moved toward the northwest, with another negative anomaly intensifying southeast from it. This coincided with the movement to the west of the heat content anomalies in the layer 300–1000 m (Figure 14d) and 1000–3000 m (Figure 15d). But note that these two layers show anomalies of opposite sign. During the integration year 5, the dipolar heat anomaly in the layer 300–1000 m (Figure 14d) further moved toward

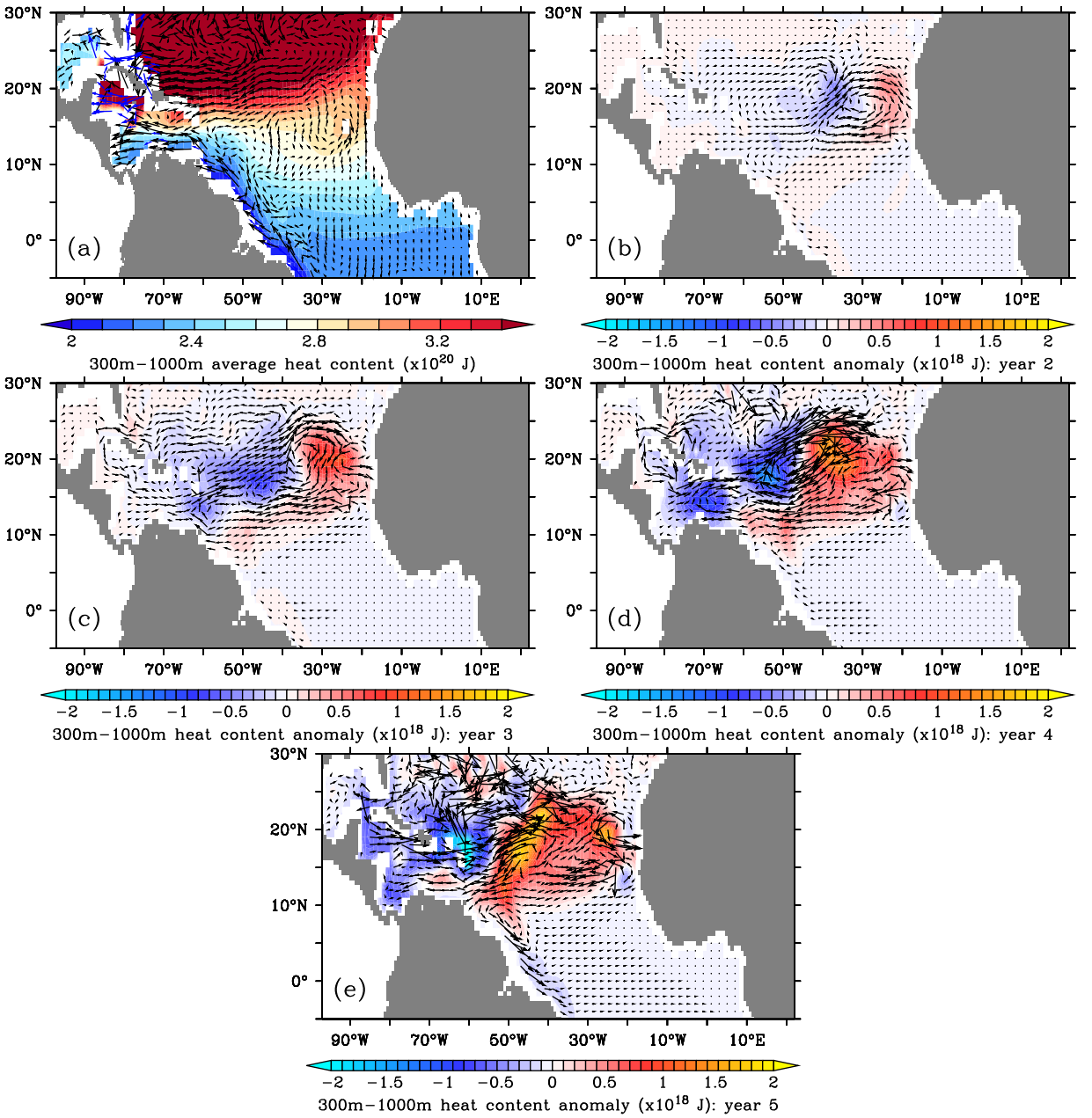

Figure 14. (a) Average 300–1000 m vertically integrated heat content in the unperturbed experiment with the 300–1000 m vertically integrated heat flux vectors superimposed. The corresponding annual anomalies (SINE experiment minus unperturbed run) are shown for years (b) 2, (c) 3, (d) 4, and (e) 5.

the Antilles. In the layer 1000–3000 m, on the other hand, the positive heat anomaly reached the continental slopes (Figure 15e) and its associated anticyclonic circulation anomaly (at 20°N, 60°W) roughly explains the shape of the anomaly in barotropic stream function (Figure 13i).

Regarding the overturning stream function anomalies $\Delta\phi$, a consistent increase south of 20°N is noticeable and a weak decrease north of this latitude is visible. This pattern persists and slowly builds over the course of the first 3 years (Figures 13b, 13d, and 13f). Interestingly, the overturning anomalies are first larger in the layer 1000–3000 m. Although the flow anomalies are not so intense as in the layers above, the layer 1000–3000 m presents mainly southward flow associated with the positive heat content anomaly (Figures 15b and 15c). At these depths, that southward flow anomaly adds to the southward flow of the Deep Western Boundary Current, thus increasing the basin-integrated transport and therefore the total overturning. In the

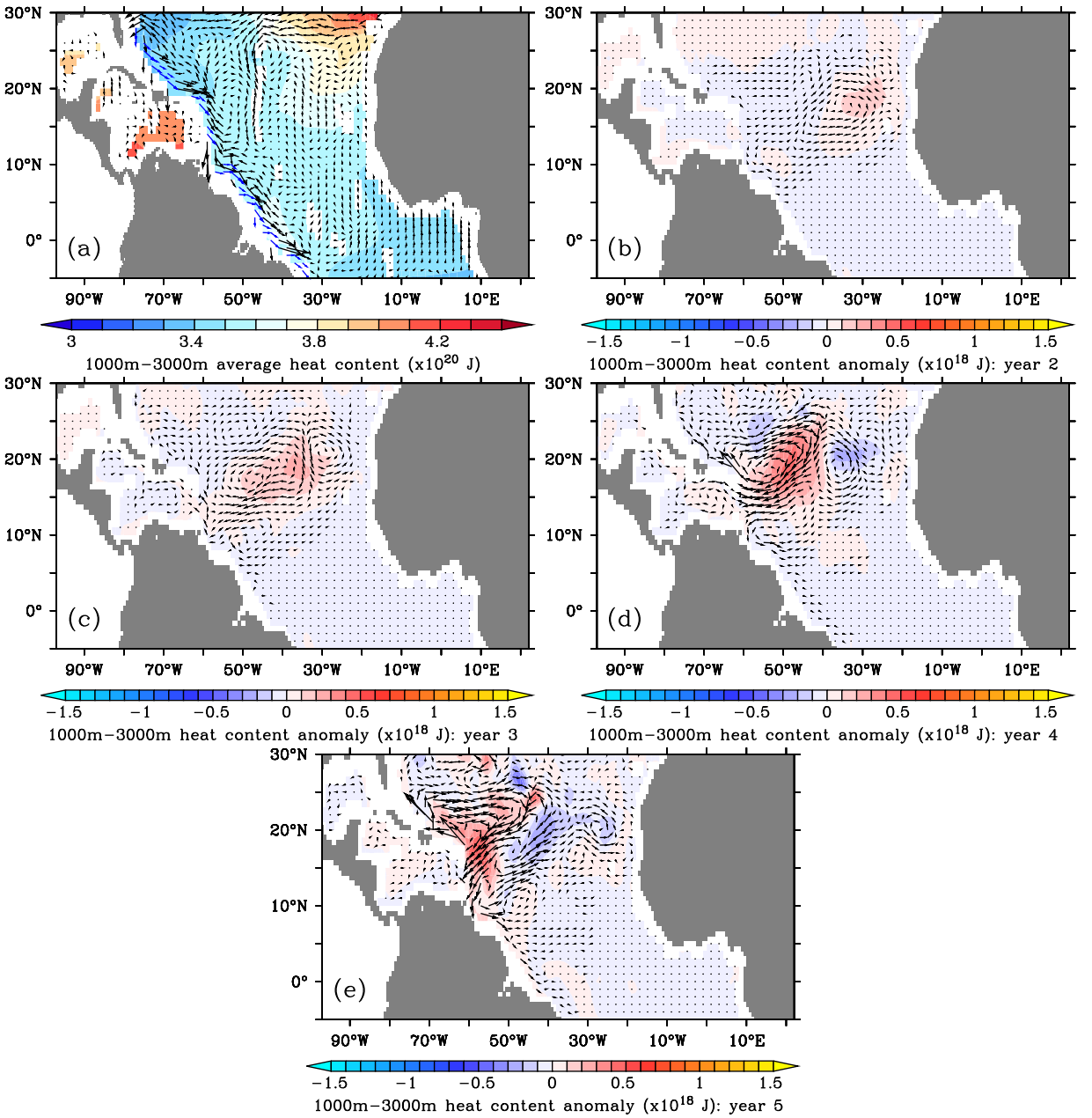

Figure 15. (a) Average 1000–3000 m vertically integrated heat content in the unperturbed experiment with the 1000–3000 m vertically integrated heat flux vectors superimposed. The corresponding annual anomalies (SINE experiment minus unperturbed run) are shown for years (b) 2, (c) 3, (d) 4, and (e) 5.

layers above there is net northward mass transport, but the strong flow anomalies are either zonal or cancel each other (e.g., Figures 14b and 14c), therefore not being detected as an overturning change.

After 4 years, the increase in overturning is mainly characterized by an increase in the upper 1000 m south of 20°N (Figures 13h and 13j), with a collocated reverse sign but weaker anomaly in the layer 1000–3000 m. That intriguing response can again be explained with the help of the layer integrated fluxes. As soon as the anomalous signals reach the western boundary, zonal cancellation of the flow around the anomalies is disrupted and different net meridional transports emerge. The upper 0–300 m layer shows in years 4 and 5 a strong response of the North Brazil Current (Figures 11d and 11e), with an enhancement of the northward flow and therefore and increase in the upper part of the overturning cell. The layer 1000—3000 m presents during year 5 the arrival of the warm anomaly to the Antilles (Figure 15e). It can be seen that northward

flow develops over the slope and at the western side of the warm anomaly. Both contribute to a reduction of the basin-integrated southward flow and thus to a reduction in overturning.

North of 40°N, the overturning anomalous signals (Figures 13h and 13j) are attributed to changes in subpolar gyre circulation and water mass formation and export to the south. However, during the course of the 5 years of integration, the overturning changes originating in the north are unrelated to that further south. In fact, latitude-time diagrams of overturning anomalies at 1000 m (not shown) present no clear propagation of signals from the subpolar gyre to regions south of the Gulf Stream.

In conclusion, the east-west anomalous density gradients generated by the buoyancy perturbation imposed in the eastern Atlantic are large enough to generate changes in the Atlantic gyre circulation and MOC. Surprisingly, the layers below the upper ocean cooling are dramatically implicated in the process, determining much of the overturning response, as the deep warming anomaly advects to the west and reaches the continental slope east of the Antilles.

6. Linearity of the Ocean Response

To investigate to which extent the ocean response is linear we conducted three additional experiments. In the first two runs we (i) doubled the amplitude of the dust-related cooling by a factor of two (experiment DOUBLE), leading to a shortwave reduction of 34 W m^{-2} and (ii) kept the amplitude of the DOUBLE perturbation but changed its sign (experiment HEAT, see Table 1 for details). In the final experiment (called AOD), the actual values of aerosol optical depth derived from satellite measurements (as opposed to a generic temporal structure) are used. The idea behind the latter experiment is to introduce a more realistic seasonal cycle together with some forcing variability at higher frequencies. The average net heat flux reduction is between that of cases SINE and DOUBLE (Table 1). Since the resulting spatial patterns of response in all cases are similar (except in terms of amplitude and sign) to the ones of SINE, they are not shown.

Results reveal that a doubling of the forcing intensity leads to a doubling of the response in the northeastern Atlantic; however, the SST and SSH spatial patterns and their evolution remain rather similar. In the case of HEAT, the patterns are similar but have the reverse sign, i.e., a warming is seen instead of a cooling and a positive SSH anomaly instead of a SSH depression. This is demonstrated in Figure 16, showing the temporal evolution of ΔSST and ΔSSH averaged between 13°N and 23°N (the latitude interval where the response is largest) separately for the western and eastern margins. The figure allows the comparison of all four experiments (black—SINE; red—DOUBLE; green—HEAT; and blue—AOD).

Shifting attention to the eastern basin (Figures 16b and 16d), a clear seasonal cycle is present in the perturbed SST and SSH from all simulations, stronger in ΔSST. The magnitude of response in all cooling experiments (SINE, DOUBLE, and AOD) reflects the magnitude of the spatial pattern imposed (see Table 1) and in the heating experiment is comparable with that from DOUBLE. The AOD response is close to the DOUBLE experiment. Since the AOD perturbation was constructed with measured AOD and a forcing efficiency computed from in situ observations, these points to the result that our DOUBLE experiment might even be a closer approximation to the true dust impact.

All experiments seem to reach an almost steady state in the eastern basin within 1 year. In contrast, the perturbations in SST and SSH remain small in the western basin during the first 2 years and then gradually increase during year 3 (Figures 16a and 16c), when the perturbation arrives at the western margin. We note, however, that in the west the ΔSST amplitude is only about 5% (and the ΔSSH amplitude is about 50%) of that in the east and that a seasonal cycle is absent.

Judging from experiments DOUBLE and HEAT, we conclude that the response remains linear during the first 4 years in both eastern and western basins. The large-scale ocean response (in terms of overturning and gyre circulations) remains also linear across the performed experiments, with doubling the forcing strength relative to the SINE experiment leading to maxima and minima twice as large in overturning and gyre anomalies. Furthermore, the experiment with high-frequency fluctuations in the shortwave anomaly forcing (experiment AOD) did not show significant changes to the anomalous patterns. Moreover, the experiment AOD (blue curves in Figure 16) reveals that the large-scale response of the ocean in a coarse-resolution model is not susceptible to short time variability in the perturbation (seen in the blue curve in Figure 2d), as

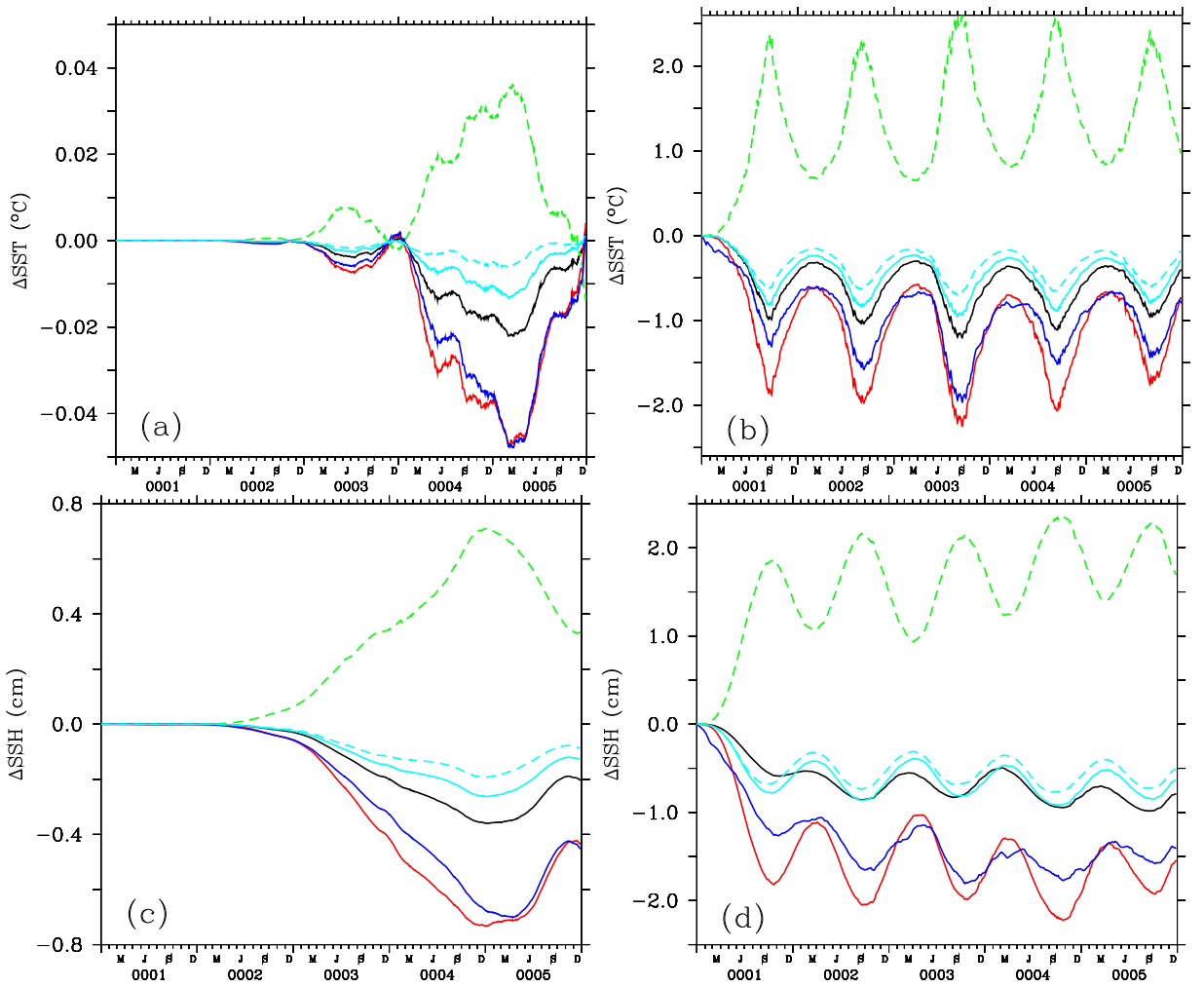

Figure 16. (a and b) ΔSST (in °C) and (c and d) ΔSSH (in cm) averaged in the latitude band 13°N–23°N (left) in the western Atlantic and (right) in the eastern Atlantic. Colors correspond to different perturbed experiments (see text): black—SINE; red—DOUBLE; green—HEAT; blue—AOD; and cyan (solid, dashed)—SINE + relaxation (180 days, 90 days).

far as it can be deduced from the relatively short model integration. That would mean that, in what concerns the ocean response, short dust outbreaks are not as important as dust seasonal signals.

As stated above, since the use of prescribed fluxes does not allow for a mechanism enabling the surface SST anomalies to be damped by air-sea interaction and, therefore, a potential exaggeration of the amplitude of the ocean response could be claimed, we performed additional experiments in which the SST of the perturbed SINE run was relaxed toward the SST from the unperturbed run. As expected, the restored experiment gave patterns of ocean response in all similar to the ones presented in previous sections and are therefore not shown. To give a range of possible ocean responses, we show the magnitude of the anomalies from the SINE runs using relaxation scales of 90 d and 180 d, which, as stated in section 2, give an SST response close to the observational/modeling estimates. The response in the east decreased very little (see cyan curves in Figures 16b and 16d) and in the west a bit larger. The difference between the ocean response magnitude from the restored and unrestored experiments is smaller in the east than the response itself, which reinforces the validity of our experimental setup.

7. Impact on the Meridional Heat Transport

The overturning and gyre circulation changes resulting from the dust-induced cooling also affect the MHT (Figure 17a), as already seen in the horizontal heat flux maps. The MHT was further split into overturning and gyre contributions and the corresponding anomalies are shown in Figures 17b and 17c, respectively.

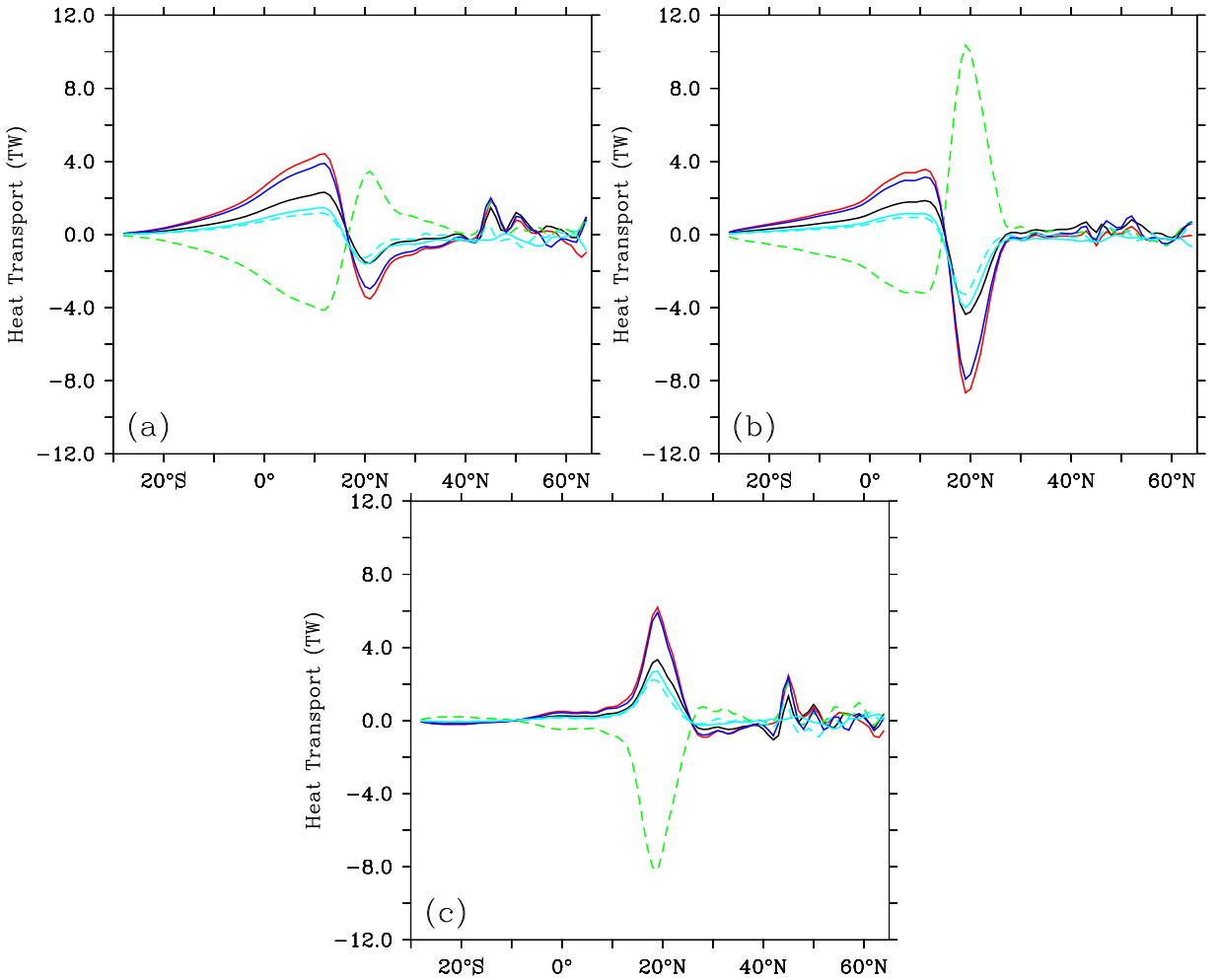

Figure 17. Anomaly (relative to the unperturbed experiment) of (a) mean total meridional heat transport for the five perturbed experiments: black—SINE; red—DOUBLE; green—HEAT; blue—AOD; and cyan (solid, dashed) —SINE + relaxation (180 days, 90 days). (b and c) Correspond, respectively, to the anomalies in mean overturning and mean gyre components of the meridional heat transport.

The overall effect of the cooling perturbation is to increase the MHT south of 15°N and to decrease it north of that latitude until about 40°N, with magnitudes differing according to the forcing strength. The changes in total MHT south of 15°N (Figure 17a) can be accounted almost solely by overturning changes (with a maximum of 2 TW in experiment SINE). The anomalies of the gyre component of MHT turn out to be relatively important between 15°N and 23°N, partly canceling the overturning negative contribution there (which amounts to −4 TW in SINE). North of 23°N, the variations in the total MHT are dominated by the gyre component and it peaks at about 45°N. This latter feature, which represents only a small fraction of the total MHT, is most likely the result of the presence of meanders in the North Atlantic Current, which are slightly different in the unperturbed and perturbed runs. It can be seen that this signal almost completely vanishes in the runs with SST damping, reinforcing the conclusion that the signal in the tropical region is not related to heat transport modification in the subpolar gyre.

The anomalies of the total MHT show a convergence of heat at the forcing latitude. This can be shown to originate from the heat stored in the tropical Atlantic. The total heat balance over the subtropical and tropical Atlantic regions (from 24°S to 40°N) is shown in Figure 18. The overall (small) cooling over the whole domain is balanced by the surface heat flux imposed in the forcing region (Figure 18a). The small cooling corresponds to a change in the storage, which over the 5 year period is four orders of magnitude smaller than the heat content in the control experiment (Figure 18b). Opposite to the heat balance below the forcing region, the Atlantic horizontal divergence is really small and only starts to play a role during year 5 (red curve in Figure 18a).

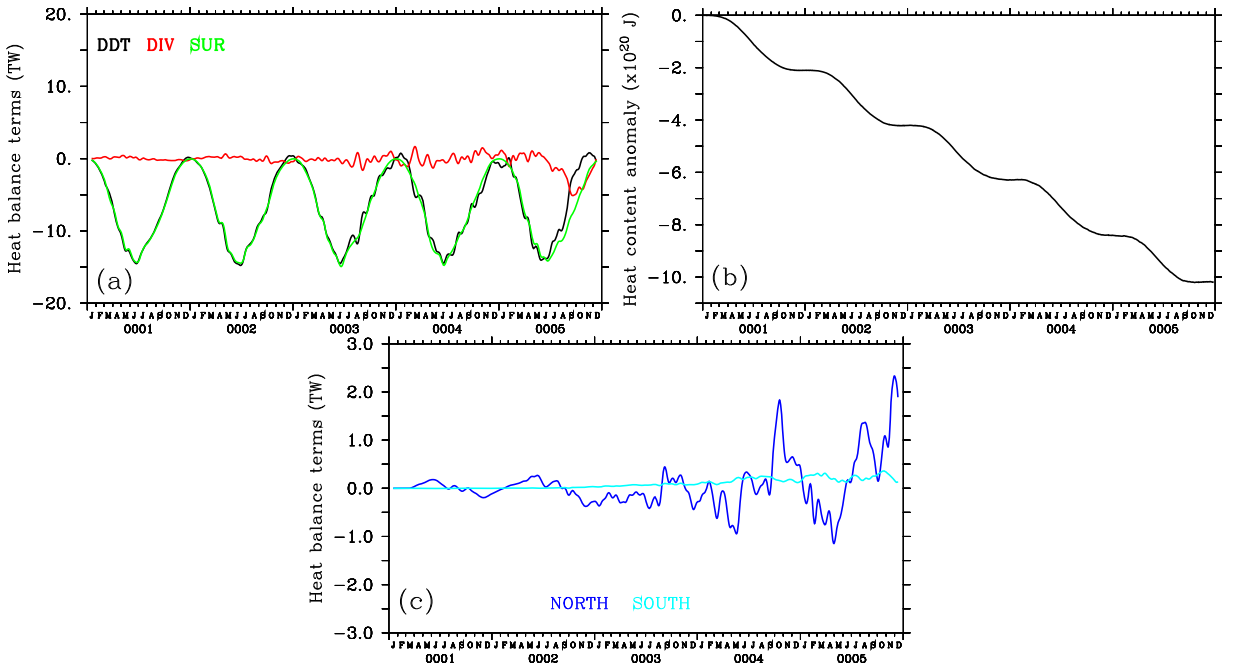

Figure 18. (a) Anomalies (perturbed minus unperturbed) of the total heat balance terms evaluated from 24°S to 40°N from the SINE experiment: black—heat content change; red—horizontal heat divergence; and green—surface heat flux. (b) Anomaly of the respective box-integrated local heat content. (c) Anomalies of the heat divergence terms: blue—northern horizontal flux at 40°N and cyan—southern boundary horizontal flux at 24°S.

The open boundary conditions in our simulations remain unchanged between unperturbed and perturbed experiments. That means that the divergence of heat in the total domain (i.e., heat flux at 65°N minus heat flux at 30°S) cannot change. However, the anomalies of these two lateral heat fluxes over the course of the 5 years are negligible (not shown); as shown in Figure 18c, they start to be relevant at 40°N only after 4 years. That was one of the reasons why the integration was stopped after 5 years. Further integration would become unrealistic since the heat fluxes to the Nordic Seas and to the Southern Ocean would start to matter. We therefore claim that the unrealism due to the open boundary condition is small during our relatively small integration time.

Finally, we would like to put the magnitude of the ocean response into context and show its relative importance. Figure 19 presents total and filtered time series of MHT in the latitudinal band 10–30°N, computed from the output of a 8 km resolution (i.e., eddy resolving) integration of an Atlantic-Arctic setup of the MITgcm forced by bulk formulae and the 1948–2009 6 h NCEP RA1 atmospheric state (further details on the model configuration can be found in *Serra et al.* [2010]). The standard deviations of all shown curves are given in the figure together with the corresponding frequency band.

The amplitude of MHT response from the AOD experiment (the one probably closer to the true response, since it uses realistic AOD and aerosol forcing efficiencies) is about 4% of the total MHT signal (above 1 year) and amounts to 14% of the MHT variability existing in the model for periods from 3 to 10 years. The lower bound of our estimates comes from the SINE run including SST relaxation of 90 days. There, the response is about 2% of the total MHT signal above 1 year and 7% of the 3–10 years MHT variability. These estimates point to the possibility of dust impacts being significant for the MHT interannual variability in the subtropical North Atlantic.

8. Discussion and Final Remarks

The goal of this work was to study the immediate changes of the North Atlantic Ocean circulation over a 5 year period forced by net shortwave heat flux modifications in the eastern part of the subtropical gyre due to Saharan dust loads in the atmosphere. We have discussed the oceanic processes relevant to understanding the ocean response to the buoyancy anomaly, namely: subduction and westward advection of

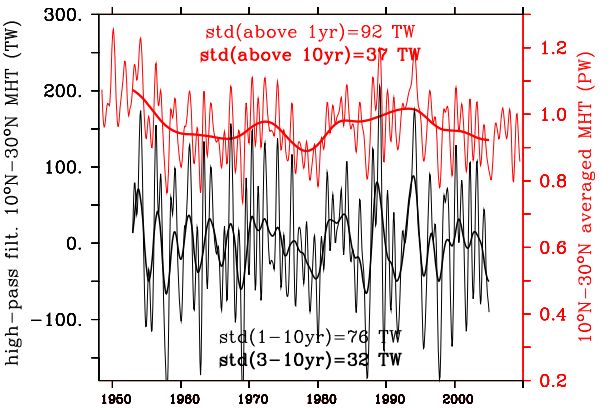

Figure 19. Atlantic meridional heat transport averaged in the latitudinal band 10°N–30°N from a 8 km resolution Atlantic-Arctic model forced by fluxes computed with bulk formulae and the 1948–2009 6 h NCEP reanalysis atmospheric state: low-pass filtered (thin red: 1 year cutoff; thick red: 10 years cutoff) and band-pass filtered (thin black: 1–10 years; thick black: 3–10 years).

anomalies in the southern part of the subtropical gyre, Kelvin wave propagation along the eastern margin with impacts on dense-water formation in the subpolar region, entrainment mixing in the base of the mixed layer under the forcing region, basin-wide density gradients and implications to the MOC, and meridional heat transport changes due to overturning and horizontal gyre modifications. The focus of the work was to bring those processes in relation to the ocean response, rather then conducting in-depth studies of each physical process separately.

The first-order impact of the reduced shortwave flux is to reduce the surface temperature and thereby to depress the ocean surface. During the first months, the local induced SST and SSH anomalies show clearly the shape of typical Saharan high dust loads. The anomalous ocean conditions start to advect westward and repeat every year triggered by the summer high-dust season. The local cooling progressively penetrates deeper in the water column, extending up to 300 m after 3 years; resulting temperature anomalies subduct toward the west and reach the western margin after about 4–5 years.

In our simulations, the surface cooling effectively densifies the ocean in the forcing region and leads to a deeper mixed layer during winter months. This is at odds with the study of *Mahowald et al*. [2011], which points toward a (slight) shallowing of the mixed layer in our forcing region, although they were expecting a deepening due to the surface cooling. Agreeing with their approach and results, the apparent inconsistency has to be attributed to the modified wind, which in their coupled ocean-atmosphere model occurs due to additional feedbacks from the cooling to the wind patterns (this is not included in our idealized ocean-only simulation). It remains to be demonstrated, however, if the wind response established in their coupled run is indeed realistic, i.e., close to the NCEP reanalyzed fields. A realistic wind field is, on the other hand, ensured in our idealized experiments by using the NCEP reanalyzed fields to force the model.

The gyre circulation changes revealed by the Atlantic barotropic stream function anomalies show a dipolar pattern associated with the cooling anomaly in the first 3 years, which is of opposite sense to the background circulation. As soon as the perturbation reaches the western margin, the response amplifies and impacts the whole subtropical gyre. The Atlantic MOC shows a general pattern of an increase south of 15°N and a decrease north of that latitude, which is collocated with the anomaly in horizontal gyre circulation. The Atlantic MHT follows the same behavior with an increase (decrease) south (north) of 15°N. The ocean response in our simulations remains linear when forced with different anomaly strengths and signals.

A new aspect in our study is the quantification of the ocean response in terms of both MOC and MHT, both important climatic quantities. Realism in our simulations is not claimed since the forcing pattern is highly idealized (although with comparable magnitude to observational estimates). Nevertheless, our perturbed experiment results point to MOC changes that after 5 years are between 0.13 Sv (SINE experiment) and 0.25 Sv (AOD experiment), i.e., about 3–6% of the standard deviation of the monthly averaged observed MOC (4.0 Sv), inferred from measurements of the RAPID array [e.g., *Cunningham et al*., 2007]. If only periods longer than 1 year are taken into account, the RAPID measurements have a standard deviation of 1.9 Sv, and so our perturbed signal would amount to 6–12% of that. Furthermore, as shown, our dust-related MHT signal is significant when compared to the variability simulated with a high-resolution model incorporating intraannual and interannual variability in the forcing of the past 62 years.

In a recent study, *Zanna et al*. [2011] inferred a significant growth of the MOC anomalies when prescribing optimal density anomalies at high latitudes and below 1000 m depth. Even though a density anomaly at

the location of the Saharan dust plume is exhibited in their Figure 3, it is confined to depths larger than 1000 m with a maximum at 3000 m. Since our buoyancy perturbation is located eastward of 25°W and it remains in the upper 500 m, *Zanna et al*. [2011] findings could serve as a possible explanation for the relatively small MOC anomalies we obtain. Moreover, the authors studied the amplification of MOC anomalies due to nonnormal linear ocean dynamics which agrees with the larger MOC response that we find in years 4 and 5 once the dust-induced perturbation deepens and arrives to higher latitudes.

The downstream response we obtained, namely off the Grand Banks of Newfoundland (the Northwest Corner), occurs even in the absence of our particular buoyancy forcing at the eastern boundary. It is a highly nonlinear region (current meandering and eddying features), which always shows a response. Although not directly relevant for our study, it shows that whatever local process changes the density structure in the subtropical gyre will have a repercussion further downstream. The anomalies at the Northwest Corner are in fact modifications in the meandering of the North Atlantic Current in the perturbed experiment. As shown, the MOC is primarily impacted at the latitude of the shortwave forcing anomaly. It is therefore to be expected that a different northward mass and heat transport will have an effect on the Gulf Stream and its extension.

Another aspect of the response is that the eastern boundary anomaly triggers a fast northward propagating Kelvin wave response along the eastern boundary. When this signal reaches high latitudes, it starts impacting the deep water formation, leading to perturbed-unperturbed differences that are small and more randomly localized. This is one of the reasons behind stopping the integration as soon as we get a large response off the Grand Banks of Newfoundland. A longer integration toward equilibrium, although possible, would suffer from longer time scale responses of the ocean (dense water formation and export out of the Labrador Sea with subsequent MOC variations), which are not of interest here and cannot be uniquely attributed to the buoyancy forcing in the eastern subtropical gyre.

In this work, it is assumed that the first-order impact of Saharan dust is on the net shortwave fluxes and therefore only this quantity was perturbed. As stated in section 2, in addition to the shortwave radiation-induced forcing incorporated in the presented simulations, the dust should account for other effects, such as enhanced longwave radiation from dust-clouds thermal emissions, changes due to dust-induced ocean fertilization, enhanced turbidity due to dust deposition/sinking and associated changes in the vertical profile of light absorption. These mechanisms were not integrated in the idealized experiment, which surely introduces an unknown uncertainty in the real ocean response. Nevertheless, a study by *Zhu et al*. [2007] found the longwave forcing efficiency at surface to be three times smaller than the shortwave one in the region. On the other hand, experiment AOD included a radiative forcing computed using a forcing efficiency estimated from observational data in the region off Africa. Interestingly, the response is close to the DOUBLE experiment. We therefore believe that the SINE experiment fully accounts for the unknown longwave attenuation of the cooling. In conclusion, the range of forcing magnitudes presented here accounts, in our opinion, to the disregarded longwave response.

There are large uncertainties concerning how the Saharan aerosol input into the ocean will vary in the future. The uncertainties arise in particular due to the difficulty in modeling the atmospheric feedbacks associated with the presence of dust and its impact on the precipitation over the Sahel region, at present the main source region of dust aerosols to the North Atlantic [*Prospero and Lamb*, 2003; *Yoshioka et al*., 2007; *Mulitza et al*., 2010; *Mahowald et al*., 2011]. Using proxy records, *Shanahan et al*. [2009] report a clear link between multidecadal Atlantic SST variability and the West African monsoon, the latter responsible for cycles of dry and wet conditions over West Africa. A future continuation of the severe drought in West Africa (known as the "Sahel drought") as a consequence of centennial-scale monsoon variability is possible. From the long record, the authors conclude that longer and more intense droughts are possible. Given these results, the magnitude of the forcing signal in our experiments might have remained conservative. In any case, the future atmospheric dust loading over the Atlantic and the associated ocean response is an aspect of climate research that needs further attention.

Acknowledgments
We thank Armin Köhl for useful discussions and the anonymous reviewers for their comments, which helped to improve the manuscript. This work was in part supported by the German BMBF funded projects "Nordatlantik" (TP 4.1) and SOPRAN (TP 1.5) and is a contribution to the DFG funded CliSAP effort of the University of Hamburg. All numerical simulations were performed at the Deutsche Klimarechenzentrum (DKRZ), Hamburg, Germany. The state estimate was provided by the ECCO Consortium for Estimating the Circulation and Climate of the Ocean funded by the National Oceanographic Partnership Program (NOPP).

References

Bryden, H. L., and S. Imawaki (2001), Ocean heat transport, in *Ocean Circulation and Climate: Observing and Modelling the Global Ocean, Int. Geophys. Ser.*, vol. *77*, edited by G. Siedler, J. Church, and J. Gould, pp. 455–474, Academic Press, London.

Chidichimo, M. P., T. Kanzow, S. A. Cunningham, W. E. Johns, and J. Marotzke (2010), The contribution of eastern-boundary density variations to the Atlantic meridional overturning circulation at 26.5°N, *Ocean Sci.*, *6*(2), 475–490, doi:10.5194/os-6-475-2010.

Christopher, S. A., and T. Jones (2007), Satellite-based assessment of cloud-free net radiative effect of dust aerosols over the Atlantic Ocean, *Geophys. Res. Lett.*, *34*, L02810, doi:10.1029/2006GL027783.
Conkright, M. E., R. A. Locarnini, H. Garcia, T. O. Brien, T. Boyer, C. Stephens, and J. Antonov (2002), *World Ocean Atlas 2001: Objective Analyses, Data Statistics, and Figures* [CD-ROM], p. 17, Natl. Oceanogr. Data Cent., Silver Spring, Md.
Cunningham, S. A., et al. (2007), Temporal variability of the Atlantic meridional overturning circulation at 26.5°N, *Science*, *317*, 935–938, doi:10.1126/science.1141304.
Evan, A. T., J. Dunion, J. A. Foley, A. K. Heidinger, and C. S. Velden (2006), New evidence for a relationship between Atlantic tropical cyclone activity and African dust outbreaks, *Geophys. Res. Lett.*, *33*, L19813, doi:10.1029/2006GL026408.
Evan, A. T., D. J. Vimont, A. K. Heidinger, J. P. Kossin, and R. Bennartz (2009), The role of aerosols in the evolution of tropical North Atlantic ocean temperature anomalies, *Science*, *324*(5928), 778–781, doi:10.1126/science.1167404.
Evan, A. T., G. R. Foltz, and D. Velden (2012), Physical response of the tropical-subtropical North Atlantic Ocean to decadal-multidecadal forcing by African dust, *J. Clim.*, *25*, 5817–5829.
Foltz, G. R., and M. J. McPhaden (2006), The role of oceanic heat advection in the evolution of tropical North and South Atlantic SST anomalies, *J. Clim.*, *19*, 6122–6138.
Foltz, G. R., and M. J. McPhaden (2008a), Impact of Saharan dust on tropical North Atlantic SST, *J. Clim.*, *21*, 5048–5060.
Foltz, G. R., and M. J. McPhaden (2008b), Trends in Saharan dust and tropical Atlantic climate during 1980–2006, *Geophys. Res. Lett.*, *35*, L20706, doi:10.1029/2008GL035042.
Greatbatch, R. J. (1994), A note on the representation of steric sea level in models that conserve volume rather than mass, *J. Geophys. Res.*, *99*, 12,767–12,771.
Hall, M. M., and H. L. Bryden (1982), Direct estimates and mechanisms of ocean heat-transport, *Deep Sea Res., Part A*, *29*, 339–359.
Heimbach, P., C. Wunsch, R. M. Ponte, G. Forget, C. Hill, and J. Utke (2011), Timescales and regions of the sensitivity of Atlantic meridional volume and heat transport: Toward observing system design, *Deep Sea Res., Part II*, *58*(17–18), 1858–1879, doi:10.1016/j.dsr2.2010.10.065.
Kalnay, E., et al. (1996), The NCEP/NCAR 40 year reanalysis project, *Bull. Am. Meteorol. Soc.*, *77*, 437–471.
Köhl, A. (2005), Anomalies of meridional overturning: Mechanisms in the North Atlantic, *J. Phys. Oceanogr.*, *35*(8), 1455–1472, doi:10.1175/JPO2767.1.
Lau, K., and K. M. Kim (2007), Cooling of the Atlantic by Saharan dust, *Geophys. Res. Lett.*, *34*, L23811, doi:10.1029/2007GL031538.
Li, F., A. M. Vogelmann, and V. Ramanathan (2004), Saharan dust aerosol radiative forcing measured from space, *J. Clim.*, *17*, 2558–2571.
Liu, X., J. Wang, and S. Christopher (2003), Shortwave direct radiative forcing of Saharan dust aerosols over the Atlantic Ocean, *Int. J. Remote Sens.*, *24*(24), 5147–5160.
Mahowald, N., K. Lindsay, D. Rothenberg, S. C. Doney, J. K. Moore, P. Thornton, J. T. Randerson, and C. D. Jones (2011), Desert dust and anthropogenic aerosol interactions in the Community Climate System Model coupled-carbon-climate model, *Biogeosciences*, *8*, 387–414.
Marotzke, J., R. Giering, K. Zhang, D. Stammer, C. Hill, and T. Lee (1999), Construction of the adjoint MIT ocean general circulation model and application to Atlantic heat transport sensitivity, *J. Geophys. Res.*, *104*, 29,529–29,547.
Marshall, J., A. Adcroft, C. Hill, L. Perelman, and C. Heisey (1997), A finite-volume, incompressible Navier Stokes model for studies of the ocean on parallel computers, *J. Geophys. Res.*, *102*, 5753–5766.
Marshall, J. C., A. J. G. Nurser, and R. G. William (1993), Inferring the subduction rate and period over the North Atlantic, *J. Phys. Oceanogr.*, *23*, 1315–1329.
Martínez Avellaneda, N., N. Serra, P. J. Minnett, and D. Stammer (2010), Response of the eastern subtropical Atlantic SST to Saharan Dust: A modelling and observational study, *J. Geophys. Res.*, *115*, C08015, doi:10.1029/2009JC005692.
Miller, R. L., and I. Tegen (1998), Climate response to soil dust aerosol, *J. Clim.*, *11*, 3247–3267.
Mulitza, S., et al. (2010), Increase in African dust flux at the onset of commercial agriculture in the Sahel region, *Nature*, *446*, 226–228, doi:10.1038/nature09213.
Myhre, G., A. Grini, J. M. Haywood, F. Stordal, B. Chatenet, D. Tanre, J. K. Sundet, and I. S. Isaksen (2003), Modeling the radiative impact of mineral dust during the Saharan Dust Experiment (SHADE) campaign, *J. Geophys. Res.*, *108*(D18), 8579, doi:10.1029/2002JD002566.
Ponte, R. M. (1999), A preliminary model study of the large-scale seasonal cycle in bottom pressure over the global ocean, *J. Geophys. Res.*, *104*, 1289–1300.
Prospero, J. M., and P. J. Lamb (2003), African droughts and dust transport to the Caribbean: Climate change implications, *Science*, *302*(5647), 1024–1027, doi:10.1126/science.1089915.
Serra, N., R. H. Käse, A. Köhl, D. Stammer, and D. Quadfasel (2010), On the low-frequency phase relation between the Denmark Strait and the Faroe-Bank Channel overflows, *Tellus, Ser. A*, *62*(4), 530–550, doi:10.1111/j.1600-0870.2010.00445.x.
Shanahan, T. M., J. T. Overpeck, K. J. Anchukaitis, J. W. Beck, J. E. Cole, D. L. Dettman, J. A. Peck, C. A. Scholz, and J. W. King (2009), Atlantic forcing of persistent drought in West Africa, *Science*, *324*, 377–380, doi:10.1126/science.1166352.
Sun, D., K. M. Lau, and M. Kafatos (2008), Contrasting the 2007 and 2005 hurricane seasons: Evidence of possible impacts of Saharan dry air and dust on tropical cyclone activity in the Atlantic basin, *Geophys. Res. Lett.*, *35*, L15405, doi:10.1029/2008GL034529.
Wang, C., S. Dong, A. Evan, G. R. Foltz, and S.-K. Lee (2012), Multidecadal covariability of North Atlantic sea surface temperature, African dust, Sahel rainfall, and Atlantic hurricanes, *J. Clim.*, *25*, 5404–5415.
Wilcox, E. M., K. M. Lau, and K.-M. Kim (2010), A northward shift of the North Atlantic Ocean Intertropical Convergence Zone in response to summertime Saharan dust outbreaks, *Geophys. Res. Lett.*, *37*, L04804, doi:10.1029/2009GL041774.
Yoon, S.-C., J.-G. Won, A. H. Omar, S.-W. Kim, and B.-J. Sohn (2005), Estimation of the radiative forcing by key aerosol types in worldwide locations using a column model and AERONET data, *Atmos. Environ.*, *39*, 6620–6630.
Yoshioka, M., N. Mahowald, A. Conley, W. Collins, D. Fillmore, C. Zender, and D. Coleman (2007), Impact of desert dust radiative forcing on Sahel precipitation: Relative importance of dust compared to sea surface temperature variations, vegetation changes, and greenhouse gas warming, *J. Clim.*, *20*, 1445–1467.
Yue, X., H. Liao, H. J. Wang, S. L. Li, and J. P. Tang (2011), Role of sea surface temperature responses in simulation of the climatic effect of mineral dust aerosol, *Atmos. Chem. Phys.*, *11*, 6049–6062.
Zanna, L., P. Heimbach, A. M. Moore, and E. Tziperman (2011), Optimal excitation of interannual Atlantic meridional overturning circulation variability, *J. Clim.*, *24*(2), 413–427, doi:10.1175/2010JCLI3610.1.
Zhang, J., S. A. Christopher, L. A. Remer, and Y. J. Kaufman (2005), Shortwave aerosol radiative forcing over cloud-free oceans from Terra: 2. Seasonal and global distributions, *J. Geophys. Res.*, *110*, D10S24, doi:10.1029/2004JD005009.
Zhu, A., V. Ramanathan, F. Li, and D. Kim (2007), Dust plumes over the Pacific, Indian, and Atlantic oceans: Climatology and radiative impact, *J. Geophys. Res.*, *112*, D16208, doi:10.1029/2007JD008427.